

Population-level Task-evoked Functional Connectivity

Kun Meng^{1,*} and Ani Eloyan¹

¹Department of Biostatistics, Brown University School of Public Health, Providence, RI 02903, USA

*Corresponding Author, e-mail: kun_meng@brown.edu, Address: 121 S. Main St, Providence, RI 02903, USA.

March 1, 2025

Abstract

Functional magnetic resonance imaging (fMRI) is a non-invasive and in-vivo imaging technique essential for measuring brain activity. Functional connectivity is used to study associations between brain regions either at rest or while study subjects perform tasks. In this paper, we propose a rigorous definition of task-evoked functional connectivity at the population level (ptFC). Importantly, our proposed ptFC is interpretable in the context of task-fMRI studies. An algorithm for estimating ptFC is provided. We present the performance of the proposed algorithm compared to existing functional connectivity estimation approaches using simulations. Lastly, we apply the proposed framework to estimate task-evoked functional connectivity in a motor-task study from the Human Connectome Project.

Keywords: AMUSE algorithm; Human Connectome Project; motor-task; weakly stationary with mean zero.

1 Introduction

Functional magnetic resonance imaging (fMRI) is a non-invasive brain imaging technique used to estimate both brain regional activity and interactions between brain regions due to its ability to detect *neuronal*

-
- The project herein was supported by Grant Number 5P20GM103645 from the National Institute of General Medical Sciences.
 - **Abbreviations:** BOLD, blood-oxygenation level-dependent; DC, dynamic connectivity; fMRI, functional magnetic resonance imaging; FC, functional connectivity; HCP, Human Connectome Project; HRF, hemodynamic response function; ptFC, task-evoked functional connectivity at the population level; ptFCE, ptFC estimation; ROI, region of interest; SLR, subject-wise linear regression; WSMZ, weakly stationary with mean zero.

activity in the entire brain simultaneously. In fMRI studies, brain signals are measured on 3D volume elements (*voxels*) during a certain period of time, and each signal is observed at discrete time points. For example, if an fMRI study lasts for 20 minutes and data are collected at every 2 seconds, that is, the time between successive brain scans referred to as *repetition time* (TR, denoted as Δ hereafter) is 2 seconds, then we obtain observations at 900 time points. It is often of interest to investigate neuronal activity. However, since neuronal activity occurs in milliseconds, it is impossible to directly observe it using fMRI technology. It is implicitly captured by *blood-oxygenation level-dependent* (BOLD) signals. When neuronal activity in a brain area occurs, it is followed by localized changes in metabolism, where the corresponding local oxygen consumption increases, and then oxygen-rich blood flows to this area. This process results in an increase in oxyhemoglobin and a decrease in deoxyhemoglobin. The BOLD signal value at each time point is the difference between the oxyhemoglobin and deoxyhemoglobin levels. The signal consisting of BOLD values across all time points measures the localized metabolic activity influenced by the local brain vasculature, and it indirectly measures the localized neuronal activity. FMRI captures BOLD signals while study subjects are either resting (resting-state fMRI) or performing tasks (task-fMRI).

Our brains are networks that can be expressed as graphs. Dependencies between activation in any two regions of the brain are referred to as *functional connectivity* (FC, [Cribben and Fiecas \(2016\)](#)). These dependencies have been widely studied, and several approaches are proposed for estimation of FC, especially at rest. Task-evoked FC is fundamentally different from resting-state FC. [Lynch et al. \(2018\)](#) show that existing estimates of task-evoked FC cannot explain differences between FC at rest and during a task. While brain FC in an individual subject is often of interest, referred to as subject-level FC, population-level estimates of FC have been proposed in the literature and used for obtaining more robust subject-level FC estimates (e.g., see [Mejia et al. \(2018\)](#)). To overcome the limitations of existing task-evoked FC estimation approaches when investigating population-level FC, we propose a novel definition of *population-level task-evoked FC* (ptFC). This definition is based on a correlation of subject-specific random effects capturing task-evoked neuronal activity. Importantly, our proposed ptFC framework takes into account the complex biological processes of the brain response to task stimuli that many existing estimators ignore.

We are interested in modeling neuronal activity and BOLD signals of a set of *subjects* ω from a population of interest. At each time point t , we denote by $Y_k(\omega; t)$ the BOLD signal value at the k^{th} node of ω 's brain. The word "node" herein refers to either a voxel or a *region of interest* (ROI). Aggregated BOLD

signals at a macro-area level are often of interest. That is, for each subject, BOLD signals are spatially averaged within pre-selected ROI and the resulting ROI-specific signals are analyzed. The BOLD signals for subject ω are represented by a K -vector-valued function $\{\mathbf{Y}(\omega; t) = (Y_1(\omega; t), \dots, Y_K(\omega; t))^T \mid t \in \mathcal{T}\}$ on \mathcal{T} , where \mathcal{T} is the collection of time indices and K is the number of nodes. Furthermore, we assume that \mathcal{T} is a compact subset of \mathbb{R} . In this paper, we model three types of signals in task-fMRI studies: (i) *stimulus signals* denoted by $N(t)$ representing the experimental designs of tasks, (ii) *task-evoked neuronal activity signals* at the k^{th} node $\Phi_k[\omega; N(t)]$ stemming solely from the task stimulus $N(t)$, where the “stimulus-to-activity” maps $\Phi_k[\omega; \bullet] : N(t) \mapsto \Phi_k[\omega; N(t)]$ depend on subjects ω , and (iii) observed BOLD signals $Y_k(\omega; t) = \Psi_k\{\omega; \Phi_k[\omega; N(t)]\}$ that are associated with the task-evoked neuronal activity $\Phi_k[\omega; N(t)]$, where the “activity-to-BOLD” maps $\Psi_k\{\omega; \bullet\} : \Phi_k[\omega; N(t)] \mapsto Y_k(\omega; t)$ are ω -dependent. In (ii) and (iii), map $\Phi_k[\omega; \bullet]$ characterizes how neurons at the k^{th} node of ω react to stimulus $N(t)$, and map $\Psi_k\{\omega; \bullet\}$ describes how neuronal activity $\Phi_k[\omega; N(t)]$ induces BOLD signal $Y_k(\omega; t)$. We are interested in modeling $\Phi_k[\omega; N(t)]$. However, only BOLD signals $Y_k(\omega; t)$ are observable. The goal of many fMRI studies, including our work, is to recover $\Phi_k[\omega; \bullet]$ by analyzing $Y_k(\omega; t)$. In Section 2, we provide nonparametric models for $\Phi_k[\omega; \bullet]$ and $\Psi_k\{\omega; \bullet\}$.

Theoretically, time t is continuous and $\mathcal{T} = [0, t^*]$, where $t^* < \infty$ denotes the end of experiment. In applications, we obtain data only at discrete and finite time points in $\mathcal{T} = \{\tau\Delta\}_{\tau=0}^T$, where Δ is the predetermined TR and T indicates that BOLD signals are observed at $T+1$ time points. A BOLD signal at the k^{th} node of subject ω in task-fMRI consists of three components: (i) $P_k(\omega; t)$ denotes the one evoked solely by the experimental task $N(t)$, (ii) $Q_k(\omega; t)$ denotes the one stemming from spontaneous brain activity, e.g., the activity coordinating respiration and heartbeat, and the neuronal activity responding to stimuli that we are not of interest, and (iii) random error $\epsilon_k(\omega; t)$. We assume that these components have an additive structure, and observed BOLD signals $Y_k(\omega; t)$ are of the following form.

$$Y_k(\omega; t) = P_k(\omega; t) + Q_k(\omega; t) + \epsilon_k(\omega; t), \quad k = 1, 2, \dots, K, \quad t \in \mathcal{T}, \quad (1.1)$$

where $P_k(\omega; t)$ are called *task-evoked terms*. $P_k(\omega; t)$ are of primary interest and identifiable under some probabilistic conditions. The proof of identifiability of $P_k(\omega; t)$ is in Appendix C. Model (1.1) is equivalent to many existing approaches for modeling BOLD signals in task-fMRI (e.g., Joel et al. (2011), Zhang et al. (2013), and Warnick et al. (2018)). The relationship between (1.1) and these approaches is discussed in Appendix A. Similar to these existing methods, we assume no interaction between $P_k(\omega; t)$ and $Q_k(\omega; t)$

in (1.1). Inclusion of an interaction between these terms is discussed in Appendix H.

We implement our proposed methods to estimate functional connectivity in a study investigating the human motor system. To investigate motor FC, we use a cohort of subjects from a task-evoked fMRI study publicly available at the Human Connectome Project (HCP). The *block-design* motor task used in this study is adapted from experiments by Buckner et al. (2011) and Yeo et al. (2011), while details on the HCP implementation are in Barch et al. (2013). During the experiment, the subjects are asked to perform five tasks when presented with a cue: tap left/right fingers, squeeze left/right toes, and move their tongue. BOLD signals $Y_k(\omega; t)$ are collected from 308 participants, and each BOLD signal is obtained with $\Delta = 0.72$ (seconds). Each experiment lasts for about 204 seconds, i.e., $T = 283$. We focus on the brain functional connectivity for the task of *squeezing right toes*. The onsets of these task blocks vary across subjects. Nevertheless, the corresponding onsets of any two participants differ in less than 0.1 seconds ($\leq \Delta$). Therefore, we assume that all subjects share the same stimulus signal $N(t) = \mathbf{1}_{[86.5, 98.5)}(t) + \mathbf{1}_{[162, 174)}(t)$.

In statistical analysis of task-fMRI data $\{\mathbf{Y}(\omega; t)\}_{t \in \mathcal{T}}$ in (1.1), two topics are primarily of interest: (i) identification of nodes presenting task-evoked neuronal activity, i.e., the indices k such that $P_k(\omega; t) \neq 0$, and (ii) detection of task-evoked associations between brain nodes. *General linear models* (GLM, Friston et al. (1994)) are commonly implemented to detect task-evoked nodes (Lindquist et al. (2008)). GLM is conducted at an individual node level and is not informative for investigating associations between nodes. Associations between nodes captured by BOLD signals characterize FC (Friston et al. (1993)). FC observed during a task experiment tends to be different from that observed in a resting-state experiment (Lowe et al. (2000)). The difference between task-fMRI and resting-state fMRI is presented by the task-evoked terms $P_k(\omega; t)$. In this paper, we investigate the associations between $\{P_k(\omega; t)\}_{k=1}^K$, instead of those between BOLD signals $\{Y_k(\omega; t)\}_{k=1}^K$, corresponding to FC stemming solely from the task of interest $N(t)$.

A considerable amount of work has been done to define and estimate FC. For example, Friston et al. (1993) defines FC as the temporal Pearson correlation between a pair of BOLD signals across time. Following this approach, one may measure task-evoked FC between $P_k(\omega; t)$ and $P_l(\omega; t)$ by the absolute value of the Pearson correlation as follows

$$|corr(\omega; P_k, P_l)| := \left| \frac{\int_{\mathcal{T}} P_k^*(\omega; t) \times P_l^*(\omega; t) \mu(dt)}{\sqrt{\int_{\mathcal{T}} |P_k^*(\omega; t)|^2 \mu(dt) \times \int_{\mathcal{T}} |P_l^*(\omega; t)|^2 \mu(dt)}} \right|, \quad (1.2)$$

where $P_{k'}^*(\omega; t) = P_{k'}(\omega; t) - \frac{1}{\mu(\mathcal{T})} \int_{\mathcal{T}} P_{k'}(\omega; s) \mu(ds)$ for $k' \in \{k, l\}$; if $\mathcal{T} = [0, T^*]$, then $\mu(dt) = dt$; if $\mathcal{T} = \{\tau\Delta\}_{\tau=0}^T$, then $\mu(dt)$ is the counting measure $\sum_{\tau \in \mathbb{Z}} \delta_{\tau\Delta}(dt)$, where $\delta_{\tau\Delta}$ is the point mass at $\tau\Delta$. There are many other approaches to defining and estimating FC, e.g., *coherence analysis* (Müller et al. (2001)) and *beta-series regression* (Rissman et al. (2004)) are widely used in FC studies. These approaches have several limitations discussed in Section 2.2 that are addressed by our proposed approach.

This paper is organized as follows. Section 2 proposes models for task-evoked neuronal activity and BOLD signals, respectively; based on these models, we propose a rigorous and interpretable definition of ptFC. Section 3 presents an algorithm for estimating ptFC. We compare the performance of our proposed algorithm with existing approaches using simulations in Section 4. In Section 5, we apply the proposed approach to estimate the ptFC during a motor task using the publicly available HCP data set. Section 6 concludes the paper.

2 Population-level Task-evoked Functional Connectivity (ptFC)

We first propose models for neuronal activity and BOLD signals at individual nodes. Using these models, we provide the definition of ptFC. Lastly, we list advantages of ptFC compared to existing approaches. Hereafter, Ω denotes a study population of interest, i.e., the collection of subjects of interest. Ω is discrete and finite. Let \mathbb{P} define a study-dependent probability on Ω . Then $(\Omega, 2^\Omega, \mathbb{P})$ is a probability space, where 2^Ω is the power set of Ω . \mathbb{E} denotes the expectation with respect to \mathbb{P} . In the HCP experiment described in Section 1, Ω represents the population of healthy adults. fMRI data are collected for each subject ω in a sample of size $n = 308$ drawn from Ω according to the underlying distribution \mathbb{P} . We estimate \mathbb{P} by empirical distribution $\frac{1}{n} \sum_{\omega} \delta_{\omega}$. The expectation and correlation with respect to this empirical distribution are the sample average and sample correlation, respectively.

2.1 Definition of ptFC

Let $h_k(t)$ denote the *hemodynamic response function* (HRF, Lindquist et al. (2008)) at the k^{th} node corresponding to the task of interest $N(t)$ and shared by all subjects $\omega \in \Omega$. For each $\omega \in \Omega$, the GLM approach essentially models the task-evoked terms in (1.1) by

$$P_k(\omega; t) = \beta_k(\omega) \times (N * h_k)(t - t_{0,k}), \quad t \in \mathcal{T}, \quad \omega \in \Omega, \quad k = 1, 2, \dots, K. \quad (2.1)$$

where $\beta_k(\omega)$ is a GLM regression coefficient representing the subject-specific random effects, $t_{0,k}$ is the latency shared by all subjects as the reaction of the k^{th} node to $N(t)$ at time t is not instantaneous, and $*$ denotes convolution. Specifically, this is a GLM with response $\{P_k(\omega; t)\}_{t \in \mathcal{T}}$ and independent variable $\{(N * h_k)(t - t_{0,k})\}_{t \in \mathcal{T}}$. The error term of the GLM is absorbed by $\{\epsilon_k(\omega; t)\}_{t \in \mathcal{T}}$ in (1.1). Task-evoked terms $P_k(\omega; t)$ in (2.1) model the neuronal activity evoked by task $N(t)$, and the subject-specific $\beta_k(\omega)$ measures the magnitude of this component. Visualizations of (2.1) are in Web Figure 9. Theoretically, latency depends on subject ω . However, in most studies, the latency is much shorter than the corresponding TR Δ , and the difference between the latency times of any two subjects is negligible. Therefore, we model the latency as $t_{0,k}$ shared by all subjects. With model (2.1), we represent the model (1.1) for BOLD signals as follows.

$$Y_k(\omega; t) = \beta_k(\omega) \times (N * h_k)(t - t_{0,k}) + R_k(\omega; t), \quad t \in \mathcal{T}, \quad k = 1, \dots, K, \quad \omega \in \Omega, \quad (2.2)$$

where $R_k(\omega; t) = Q_k(\omega; t) + \epsilon_k(\omega; t)$ are referred to as *reference terms* for succinctness.

Task-evoked terms $P_k(\omega; t) = \beta_k(\omega) \times (N * h_k)(t - t_{0,k}) = [\{\beta_k(\omega) \times N(\cdot - t_{0,k})\} * h_k](t)$ correspond to neuronal activity evoked by $N(t)$, where h_k represent metabolism and vasculature and do not characterize neuronal activity. Therefore, we model neuronal activity signals $\Phi_k[\omega; N(t)]$ responding to $N(t)$ as $\beta_k(\omega) \times N(t - t_{0,k})$. Using model (2.2), the “stimulus-to-activity” map $\Phi_k[\omega; \bullet]$ and “activity-to-BOLD” map $\Psi_k\{\omega; \bullet\}$ in Section 1 are $\Psi_k\{\omega; \bullet\} : \Phi_k[\omega; N(t)] \mapsto \{\Phi_k[\omega; N(\cdot)] * h_k\}(t) + Q_k(\omega; t) + \epsilon_k(\omega; t) = Y_k(\omega; t)$ and

$$\Phi_k[\omega; \bullet] : N(t) \mapsto \beta_k(\omega) \times N(t - t_{0,k}). \quad (2.3)$$

FC is anticipated to characterize the mechanism of neuronal activity rather than metabolism or vasculature. Therefore, task-evoked FC is defined using task-evoked neuronal activity signals $\Phi_k[\omega; N(t)]$. In model (2.3) of $\Phi_k[\omega; N(t)]$, tasks $N(t)$ are fully determined by experimental designs. Additionally, latency $t_{0,k}$ can be viewed as a parameter of HRF h_k since task-evoked terms can be expressed as $\{[\beta_k(\omega) \times N] * [h_k(\cdot - t_{0,k})]\}(t)$. Therefore, task-evoked FC is expected to be determined by $\beta_k(\omega)$. Since $\beta_k(\omega)$, for $k = 1, \dots, K$, measure the magnitude of the neuronal activity evoked by task $N(t)$, nodes k and l are functionally connected at the population level during the task if one of the following scenarios holds: (i) for subjects with strong reaction to $N(t)$ at their k^{th} nodes, their l^{th} nodes’ reaction to $N(t)$ is strong as well and vice versa; (ii) for subjects with strong reaction to $N(t)$ at their k^{th} nodes, their l^{th} nodes’ reaction

to $N(t)$ is weak and vice versa, i.e., either positively or negatively correlated. Therefore, we make the following assumptions on the distribution of $\beta_k(\omega)$ across (Ω, \mathbb{P}) : (1) if there exists a functional connection evoked by $N(t)$ between nodes k and l , the corresponding $\beta_k(\omega)$ and $\beta_l(\omega)$ are approximately *linearly* associated; (2) each variance $\mathbb{V}\beta_k = \mathbb{E}(\beta_k^2) - (\mathbb{E}\beta_k)^2 > 0$, i.e., random variable $\beta_k(\omega)$ is not deterministic, where $\mathbb{E}\beta_k^\nu = \int_{\Omega} \{\beta_k(\omega)\}^\nu \mathbb{P}(d\omega)$ for $\nu = 1, 2$. Since $\text{corr}(\beta_k, \beta_l) := \frac{\mathbb{E}(\beta_k\beta_l) - (\mathbb{E}\beta_k)(\mathbb{E}\beta_l)}{\sqrt{\mathbb{V}\beta_k \times \mathbb{V}\beta_l}}$ measures the linear correlation between $\beta_k(\omega)$ and $\beta_l(\omega)$, we define ptFCs as follows.

Definition 2.1. For each subject $\omega \in \Omega$, the task-evoked BOLD signals $\{Y_k(\omega; t)\}_{k=1}^K$ are of form (2.2). The ptFC between the k^{th} and l^{th} nodes is defined as $|\text{corr}(\beta_k, \beta_l)|$.

An advantage of ptFC is its scale-invariance. Since $\beta_k(\omega)(N * h_k) = \frac{\beta_k(\omega)}{c_1 \times c_2} [(c_2 N) * (c_1 h_k)]$, the scale of $\beta_k(\omega)$ changes if the scale of h_k or $N(t)$ changes. But $|\text{corr}(\beta_k, \beta_l)|$ is invariant to the transform $\beta_{k'}(\omega) \mapsto c\beta_{k'}(\omega)$, for $k' \in \{k, l\}$ and any $c \neq 0$. Furthermore, using this scale-invariance, we show in Appendix C that ptFC is identifiable under some probabilistic conditions. Additionally, $|\text{corr}(\beta_k, \beta_l)|$ is invariant to the transform $\beta_{k'}(\omega) \mapsto \beta_{k'}(\omega) + c$ for $k' \in \{k, l\}$ and any $c \in \mathbb{R}$, hence we may assume $\mathbb{E}\beta_{k'} = 0$ for $k' \in \{k, l\}$ in Section 3.

Interpretation of $\beta_k(\omega)$: Each signal $\Phi_k[\omega; N(t)] = \beta_k(\omega) \times N(t - t_{0,k})$ describes the neuronal activity evoked by task $N(t)$, excluding effects of local vasculature or metabolism. If the k^{th} node of ω does not react to task $N(t)$, then $\beta_k(\omega) = 0$. For given $N(t)$ and h_k , the magnitude of $|\beta_k(\omega)|$ indicates the strength of the reaction in k^{th} node of ω to $N(t)$.

Interpretation of $|\text{corr}(\beta_k, \beta_l)|$: The pair $\{\beta_k(\omega), \beta_l(\omega)\}_{\omega \in \Omega}$ quantifies the magnitude of neuronal activity in response to $N(t)$ for nodes k and l . These two nodes have functional connectivity evoked by $N(t)$ if $\{\beta_k(\omega)\}_{\omega \in \Omega}$ and $\{\beta_l(\omega)\}_{\omega \in \Omega}$ are linearly associated across (Ω, \mathbb{P}) . More explicitly, a perfectly linear relationship between $\{\beta_k(\omega)\}_{\omega \in \Omega}$ and $\{\beta_l(\omega)\}_{\omega \in \Omega}$ implies strongest functional connectivity between nodes k and l evoked by $N(t)$. Finally, $|\text{corr}(\beta_k, \beta_l)|$ quantifies the strength of $N(t)$ -induced connectivity.

The proposed framework for estimation of population-level FC results in interpretable quantification of FC based on a more realistic model of task-evoked neuronal activity relationships between brain nodes compared with the existing methods discussed in Section 2.2. The Pearson correlation approach defines FC between two brain nodes by the correlation defined on time index space \mathcal{T} (see equation (1.2)). In contrast, ptFC in Definition 2.1 is of a correlation form defined on the population space Ω . Although the \mathcal{T} -correlation and Ω -correlation forms are different from the mathematical perspective, they model the same brain activity mechanism. Therefore, the correlations are comparable.

Recently, there is an emerging consensus in the literature suggesting that brain networks undergo

temporal fluctuations corresponding to experimental tasks. *Dynamic connectivity* (DC) is a collection of approaches investigating these fluctuations. Although ptFC in Definition 2.1 does not change over time, the ptFC framework can be directly incorporated to obtain *sliding-window* based DC estimates (Hutchison et al. (2013)). Specifically, for a preselected window of time, BOLD signals are extracted for that time interval, and ptFC is estimated using the algorithm proposed in this paper. Next, the window is shifted in time for a certain number of time points, and ptFC is estimated for BOLD signals within the time interval of the same length as in the first step for the shifted time interval. As a result, we obtain a sequence of ptFCs illustrating the dynamic structure of FC.

2.2 Advantages of ptFC

In this subsection, we present advantages of ptFC in Definition 2.1 compared to existing approaches. We first discuss the limitations of Pearson correlation approach (1.2) using model (2.1). Plugging (2.1) into (1.2), we obtain the following association between $P_k(\omega; t)$ and $P_l(\omega; t)$.

$$|corr(\omega; P_k, P_l)| = \left| \frac{\int_{\mathcal{T}} \phi_k(t) \times \phi_l(t) \mu(dt)}{\sqrt{\int_{\mathcal{T}} |\phi_k(t)|^2 \mu(dt) \times \int_{\mathcal{T}} |\phi_l(t)|^2 \mu(dt)}} \right|, \quad (2.4)$$

where $\phi_{k'}(t) = N * h_{k'}(t - t_{0,k'}) - \frac{1}{\mu(\mathcal{T})} \int_{\mathcal{T}} N * h_{k'}(s - t_{0,k'}) \mu(ds)$ for $k' \in \{k, l\}$. (2.4) reveals the following limitations of Pearson correlation approach (1.2).

Only nuisance parameters: Based on the reasoning in Section 2.1, task-evoked neuronal activity is modeled by $\beta_k(\omega)$. Hence, it is counterintuitive that (2.4) does not depend on $\beta_k(\omega)$ and depends only on the nuisance parameters $N(t)$ and $h_k(t)$ when considering neuronal activity. For example, if the k^{th} node does not react to $N(t)$, then the task-evoked term $\beta_k(\omega) \times (N * h_k)(t - t_{0,k})$ is expected to be zero, i.e., $\beta_k(\omega) = 0$, and there should be no task-evoked interaction between the k^{th} and other nodes. However, (2.4) can still be very large as the non-reaction information presented by $\beta_k(\omega) = 0$ vanishes. In contrast with (2.4), Definition 2.1 is based on $\{(\beta_k(\omega), \beta_l(\omega)) | \omega \in \Omega\}$.

Variation in latency: $t_{0,k}$ may vary across nodes, e.g., see Miezin et al. (2000) for investigation of the left and right visual and motor cortices and the corresponding difference between response onsets. If $t_{0,k} \neq t_{0,l}$, for example $t_{0,k} < t_{0,l}$, then it is likely that node k reacts to task $N(t)$ first, and then the neuronal activity at node k causes that at node l . Because of this potential causality represented by $t_{0,k} < t_{0,l}$, it is natural to expect that nodes k and l are likely functionally connected. However, measurement (2.4) can be very small if $t_{0,k} \neq t_{0,l}$ and may not reveal the true interaction between

neuronal activity of two nodes. An example of this issue is illustrated in Appendix F. Since our proposed ptFCs do not involve latency, the variation in latency does not influence ptFCs in Definition 2.1.

Variation in HRFs: HRFs can heavily vary across brain nodes (Miezin et al. (2000)). Since task-evoked FC is not expected to depend on HRFs, variation of HRFs in different brain regions should not influence task-evoked FC. However, (2.4) can be small if $h_k \neq h_l$ as illustrated in Web Figure 9 (c). Given that ptFCs do not involve HRFs, they are invariant to the variation in HRFs across brain nodes.

Coherence analysis for FC is not influenced by any of the issues discussed above. In this approach, FC between BOLD signals $Y_k(\omega; t)$ and $Y_l(\omega; t)$ is measured by the *coherence* evaluating the extent of the *linear time-invariant relationship* between these two signals via Fourier frequencies. However, there is no guarantee that two BOLD signals are linear time-invariant if the corresponding two nodes are functionally connected. Last but not least, the Pearson correlation and coherence analysis approaches are designed to measure FC evoked by all stimuli - both the tasks of interest and nuisance stimuli. Hence, they are not interpretable from the task-evoked FC viewpoint. On the contrary, beta-series regression and ptFCs are designed to measure the FC evoked by an experiment’s specific task of interest. Additionally, our simulation studies in Section 4 show that beta-series regression performs worse than our proposed ptFC approach in many cases.

3 ptFC Estimation (ptFCE) Algorithm

Since BOLD signals are observed at discrete and finite time points, we assume $\mathcal{T} = \{\tau\Delta\}_{\tau=0}^T$ and $t = \tau\Delta$ for $\tau \in \{0, 1, \dots, T\}$. To estimate $|corr(\beta_k, \beta_l)|$, one needs the task-evoked terms $P_k(\omega; t)$. However, these terms are not observed in most applications. In Section 3.1, we propose an estimator defined as $\tilde{R}_k(\omega; t)$ for $R_k(\omega; t)$. As a result, we can obtain estimators for task-evoked terms as $\tilde{P}_k(\omega; t) := Y_k(\omega; t) - \tilde{R}_k(\omega; t)$. Suppose h_k and $t_{0,k}$ are known, then a straightforward approach to estimate $|corr(\beta_k, \beta_l)|$ is the subject-wise linear regression (SLR) as follows: For each fixed ω , we regress $\{\tilde{P}_k(\omega; \tau\Delta)\}_{\tau=0}^T$ on $\{(N * h_k)(\tau\Delta - t_{0,k})\}_{\tau=0}^T$ without intercept, and the ordinary least squares estimator for subject-dependent coefficient $\beta_k(\omega)$ is denoted as $\tilde{\beta}_k(\omega)$; then $|corr(\beta_k, \beta_l)|$ is estimated by the absolute value of the sample correlation between $\tilde{\beta}_k(\omega)$ and $\tilde{\beta}_l(\omega)$ across all ω . However, the SLR approach is not robust to the violation of assumptions in the model (2.2) and leads to worse performance of this approach compared to our proposed method as we present in Section 4 using simulations.

To obtain a better estimator of ptFC, in this section, we propose the ptFCE algorithm based on the Fourier transform and the AMUSE algorithm (Tong et al. (1991)). First, we provide notations for the

Fourier transform. For any function $f : \mathcal{T} \rightarrow \mathbb{R}$, we extend f as follows to be a periodic function on $\{\tau'\Delta\}_{\tau' \in \mathbb{Z}}$.

$$f(\tau'\Delta) = f(\tau\Delta), \quad \tau' \equiv \tau \pmod{T+1} \text{ for } \tau = 0, 1, \dots, T \text{ and all } \tau' \in \mathbb{Z}. \quad (3.1)$$

Hereafter, all functions on \mathcal{T} are implicitly extended using (3.1) to be periodic functions on $\{\tau'\Delta\}_{\tau' \in \mathbb{Z}}$.

Convolution

$$(N * h_k)(\tau\Delta) := \frac{1}{T+1} \sum_{\tau'=0}^T N(\tau'\Delta) h_k((\tau - \tau')\Delta), \quad \text{for } \tau = 0, 1, \dots, T.$$

We define the Fourier transform of f as $\widehat{f}(\xi) := \frac{1}{T+1} \sum_{\tau=0}^T f(\tau\Delta) e^{-2\pi i \xi(\tau\Delta)}$ for $\xi \in \mathbb{R}$. $\widehat{f}(\xi)$ is a periodic function with period $1/\Delta$. Throughout this paper, $\widehat{(\cdot)}$ denotes the Fourier transform. Additionally, we assume $\mathbb{E}\beta_k = \mathbb{E}R_k(t) = 0$, for all k and t , motivated by the centralization

$$Y_k(\omega; t) - \mathbb{E}Y_k(t) = \{\beta_k(\omega) - \mathbb{E}\beta_k\} (N * h_k)(t - t_{0,k}) + \{R_k(\omega; t) - \mathbb{E}R_k(t)\}.$$

Using $\{\beta_k(\omega) - \mathbb{E}\beta_k\}$ and $\{R_k(\omega; t) - \mathbb{E}R_k(t)\}$ as $\beta_k(\omega)$ and $R_k(\omega; t)$, respectively, we model the demeaned signals $Y_k(\omega; t) - \mathbb{E}Y_k(t)$. Because of the invariance $\text{corr}(\beta_k, \beta_l) = \text{corr}((\beta_k - \mathbb{E}\beta_k), (\beta_l - \mathbb{E}\beta_l))$, the assumption $\mathbb{E}\beta_k = 0$ does not prevent the detection of ptFC $|\text{corr}(\beta_k, \beta_l)|$.

Our proposed ptFC depends on neither latency $t_{0,k}$ nor reference terms $R_k(\omega; t)$. We note that, applying periodic extension (3.1) to $(N * h_k)$, one may verify that the two stochastic processes $(N * h_k)(t - t_{0,k} - U(\omega))$ and $(N * h_k)(t - U(\omega))$, where the random variable $U : \Omega \rightarrow \mathcal{T}$ is uniformly distributed on \mathcal{T} , are identically distributed. Then $(N * h_k)(t - U(\omega))$, and hence the distribution of $(N * h_k)(t - t_{0,k} - U(\omega))$, does not depend on $t_{0,k}$. Therefore, we investigate the time-shifted signals $Y_k(\omega; t - U(\omega)) = \beta_k(\omega)(N * h_k)(t - t_{0,k} - U(\omega)) + R_k(\omega; t - U(\omega))$, for $k = 1, \dots, K$. Based on the discussion above, the distributions of $Y_k(\omega; t - U(\omega))$ do not depend on $t_{0,k}$. Then, we consider the autocovariance $\mathbb{E}\{Y_k(t - U)Y_l(t + s - U)\}$ when estimating $|\text{corr}(\beta_k, \beta_l)|$, where $s = \underline{s}\Delta$ with $\underline{s} \in \mathbb{Z}$. Additionally, $|\text{corr}(\beta_k, \beta_l)|$ depends only on task-evoked terms $\{Y_k(\omega; t - U(\omega)) - R_k(\omega; t - U(\omega))\}$ (see (2.2)). Hence, we investigate the autocovariance difference $\mathbb{E}\{Y_k(t - U)Y_l(t + s - U)\} - \mathbb{E}\{R_k(t - U)R_l(t + s - U)\}$. If $U(\omega)$, $\{\beta_k(\omega)\}_{k=1}^K$, and $\{R_k(\omega; t) | t \in \mathcal{T}\}_{k=1}^K$ are independent, Web Theorem B.1 implies that this

difference depends only on s , rather than t . Therefore, we denote it as follows.

$$\mathcal{A}_{kl}(s) = \mathbb{E}\{Y_k(t-U)Y_l(t+s-U)\} - \mathbb{E}\{R_k(t-U)R_l(t+s-U)\}, \quad k, l = 1, \dots, K. \quad (3.2)$$

We propose the following for $\xi \in \mathbb{R}$

$$\mathcal{C}_{kl}(\xi) := |\widehat{\mathcal{A}}_{kl}(\xi)| / \sqrt{|\widehat{\mathcal{A}}_{kk}(\xi)\widehat{\mathcal{A}}_{ll}(\xi)|}$$

by incorporating a normalization multiplier in (3.2). Web Theorem B.1 implies the following representation of ptFC.

$$\mathcal{C}_{kl}(\xi) = |\text{corr}(\beta_k, \beta_l)|, \quad \text{for } \xi \in \mathbb{R}. \quad (3.3)$$

The representation (3.3) motivates the ptFCE algorithm. Instead of estimating $|\text{corr}(\beta_k, \beta_l)|$, we propose estimating $\mathcal{C}_{kl}(\xi)$. The main steps of our proposed ptFCE algorithm provide estimation of factors $\mathcal{A}_{kl}(s)$ of $\mathcal{C}_{kl}(\xi)$, for $k, l \in \{1, \dots, K\}$.

BOLD signals $Y_k(\omega; t)$ are observed in experiments, and $U(\omega)$ is an auxiliary variable artificially generated in our estimation procedure (step 1 of Algorithm 1). Hence, the first term of (3.2) can be estimated using the method of moments. However, the reference signals $R_k(\omega; t)$ implicitly contained in $Y_k(\omega; t) = P_k(\omega; t) + R_k(\omega; t)$ are not observable. Section 3.1 provides the estimation of $R_k(\omega; t)$.

3.1 The Estimation of Reference Signals

In this subsection, we derive an approximation $\tilde{R}_k(\omega; t) \approx R_k(\omega; t)$ from observed $Y_k(\omega; t)$. We start by introducing the following concept: a stochastic process $\mathbf{G}(\omega; t) = (G_1(\omega; t), \dots, G_K(\omega; t))^T$ is called *weakly stationary with mean zero* (WSMZ) if $\mathbb{E}G_k(t) = 0$, for all $t \in \mathcal{T}$, and $\mathbb{E}\{G_k(t)G_l(t+s)\}$ depends only on s , rather than t , for all $k, l \in \{1, \dots, K\}$.

First, we note that $C_k := \mathbb{E}\{(N * h_k)(t - t_{0,k} - U)\}$ is a constant depending on neither t nor $t_{0,k}$. Define stochastic processes $J_k(\omega; t) = \beta_k(\omega)\{(N * h_k)(t - t_{0,k} - U(\omega)) - C_k\}$, for $k = 1, \dots, K$. For each fixed k , one can verify that scalar-valued stochastic process $J_k(\omega; t)$ is WSMZ conditioning on β_k , then $\mathbb{E}\{J_k(t)J_k(t+s)|\beta_k\}$ depends only on s . The following theorem gives the foundation for the estimation of reference terms $R_k(\omega; t)$.

Theorem 3.1. *For each $k \in \{1, \dots, K\}$, suppose that BOLD signals $Y_k(\omega; t)$ are of form (2.2), the*

scalar-valued stochastic process $\{R_k(\omega; t)\}_{t \in \mathcal{T}}$ is WSMZ, and the random variable $U : \Omega \rightarrow \mathcal{T}$ is uniformly distributed. Additionally, for each k , $\beta_k(\omega)$, $\{R_k(\omega; t)\}_{t \in \mathcal{T}}$, and $U(\omega)$ are independent, and there exist $t^* \in \mathcal{T}$ and $\beta^* \in \mathbb{R}$ so that $\frac{\mathbb{E}\{J_k(t)J_k(t-t^*)|\beta_k=\beta^*\}}{\mathbb{E}\{J_k(t)^2|\beta_k=\beta^*\}} \neq \frac{\mathbb{E}\{R_k(t-U)R_k(t-t^*-U)\}}{\mathbb{E}\{R_k(t-U)^2\}}$. If nonsingular matrix $\mathbf{A} = (a_{ij})_{1 \leq i, j \leq 2}$ and stochastic process $\{\mathbf{s}(\omega; t) = (s_1(\omega; t), s_2(\omega; t))^T\}_{t \in \mathcal{T}}$ satisfy (i) given $\beta_k(\omega) = \beta^*$, $\mathbf{s}(\omega; t)$ is WSMZ, (ii) $s_1(\omega; t_1)$ and $s_2(\omega; t_2)$ are uncorrelated for $t_1, t_2 \in \mathcal{T}$, (iii) $\frac{\mathbb{E}\{s_1(t)s_1(t-t^*)|\beta_k=\beta^*\}}{\mathbb{E}\{s_1(t)|\beta_k=\beta^*\}} \neq \frac{\mathbb{E}\{s_2(t)s_2(t-t^*)|\beta_k=\beta^*\}}{\mathbb{E}\{s_2(t)|\beta_k=\beta^*\}}$, and $\mathbf{A}(s_1(\omega; t), s_2(\omega; t))^T = (Y_k(\omega; t - U(\omega)) - \beta^*C_k, (N * h_k)(t - t_{0,k} - U(\omega)) - C_k)^T$ for $t \in \mathcal{T}$ then there exist a non-singular diagonal matrix $\mathbf{\Lambda}$ and a permutation matrix \mathbf{P} , such that

$$\begin{pmatrix} 1 & 1 \\ \frac{1}{\beta^*} & 0 \end{pmatrix} = \mathbf{A}\mathbf{\Lambda}^{-1}\mathbf{P}^{-1} \text{ and } \begin{pmatrix} J_k(\omega; t) \\ R_k(\omega; t - U(\omega)) \end{pmatrix} = \mathbf{P}\mathbf{\Lambda}\mathbf{s}(\omega; t), \text{ for all } t \in \mathcal{T}. \quad (3.4)$$

Theorem 3.1 herein is a straightforward result of the Theorem 2 in Tong et al. (1991). For each fixed k and ω with setting $\beta^* = \beta_k(\omega)$, the pair $(\mathbf{A}, \mathbf{s}(\omega; t))$ in Theorem 3.1 is derived by the AMUSE algorithm with 2D signal

$$\left\{ (Y_k(\omega; t - U(\omega)) - \beta^*C_k, (N * h_k)(t - t_{0,k} - U(\omega)) - C_k)^T \right\}_{t \in \mathcal{T}}$$

as its input. However, coefficient $\beta^* = \beta_k(\omega)$ is unknown. Since $\mathbb{E}\beta_k = 0$, we ignore $\beta_k^*C_k$ and apply the following vector-valued signal as input of the AMUSE algorithm.

$$\left\{ (Y_k(\omega; t - U(\omega)), (N * h_k)(t - t_{0,k} - U(\omega)) - C_k)^T \mid t \in \mathcal{T} \right\}. \quad (3.5)$$

The choice of latency $t_{0,k}$ and HRFs h_k in (3.5) is of importance. In our implementation of (3.5) in HCP analysis, we choose $t_{0,k} = 0$, for all k , based on the following considerations: (i) latency times are usually much smaller than their corresponding experimental time units Δ (e.g., see Zhang et al. (2013) (p 138)); (ii) latency $t_{0,k}$ can be incorporated into the corresponding HRF h_k as its parameter, i.e., we view $h_k(\cdot - t_{0,k})$ as an HRF, then the choice of $t_{0,k}$ is equivalent to the choice of corresponding HRF; (iii) The HCP data are from a block design; if latency $t_{0,k}$ are much shorter than the length of task blocks, $t_{0,k}$ are negligible. Additionally, we choose h_k in (3.5) to be the canonical HRF (the R function `canonicalHRF` with default parameters in package `neuRosim`), for all k , in our analysis of the HCP data, since in block-design experiments, the influence of biased HRFs on the ptFCE algorithm is moderate as we illustrate using simulations in Section 4; this holds even if the support of biased HRFs is longer than task blocks. Finally, $t_{0,k}$ and h_k can be estimated using data-adaptive approaches, e.g., the spline-based

method by Zhang et al. (2013). In general, given an algorithm for estimating $t_{0,k}$ and h_k , one may simply use the estimated $t_{0,k}^{est}$ and h_k^{est} as input in (3.5). Since the distribution of $U(\omega)$ is known, constants C_k can be estimated. To approximately recover $R_k(\omega; t)$ from $(\mathbf{A}, \mathbf{s}(\omega; t))$, we show the following result.

Theorem 3.2. *For each $k \in \{1, \dots, K\}$ and $\omega \in \Omega$, suppose the pair $(\mathbf{A}, \mathbf{s}(\omega; t))$ satisfies (3.4). Then there exists $i' \in \{1, 2\}$ such that $a_{1i'}s_{i'}(\omega; t) = J_k(\omega; t)$.*

The proof of Theorem 3.2 is in Appendix B. The index i' in Theorem 3.2 can be computed as

$$i' = \underset{i}{\operatorname{argmax}} \{ \operatorname{corr}(s_i(\omega; t), (N * h_k)(t - t_{0,k} - U(\omega_j))) - C_k \}, \text{ across } t | i = 1, 2 \}.$$

The AMUSE algorithm and Theorem 3.2 recover $J_k(\omega; t) = \beta_k(\omega)(N * h_k)(t - t_{0,k} - U(\omega)) - \beta_k(\omega)C_k$. Again, we ignore $\beta_k(\omega)C_k$ as $\mathbb{E}\beta_k = 0$, that is, $J_k(\omega; t) \approx \beta_k(\omega)(N * h_k)(\omega; t - t_{0,k} - U(\omega))$. Then we estimate $R_k(\omega; t - U(\omega))$ by $\tilde{R}_k(\omega; t - U(\omega)) := Y_k(\omega; t - U(\omega)) - J_k(\omega; t) \approx R_k(\omega; t - U(\omega))$, for all k and ω . In applications, $U(\omega)$ are artificially generated and known. Then we have the approximation $\tilde{R}_k(\omega; t) \approx R_k(\omega; t)$. We conclude the derivation of $\tilde{R}_k(\omega; t)$ from $Y_k(\omega; t)$ as follows: Step 1, each observed signal $Y_k(\omega; t)$ provides input (3.5) for the AMUSE algorithm; Step 2, the AMUSE algorithm computes $(\mathbf{A}, \mathbf{s}(\omega; t))$; Step 3, Theorem 3.2 indicates $J_k(\omega; t) = a_{1i'}s_{i'}(\omega; t)$; Step 4, compute $\tilde{R}_k(\omega; t)$ using $J_k(\omega; t)$ and the artificially generated $U(\omega)$.

3.2 The Estimator for $C_{kl}(\xi)$ and The ptFCE Algorithm

With observed signals $\{Y_{k'}(\omega; t) | k' = k, l\}_{\omega=1}^n$ and the signals $\{\tilde{R}_{k'}(\omega; t) | k' = k, l\}_{\omega=1}^n$ derived from $\{Y_{k'}(\omega; t) | k' = k, l\}_{\omega=1}^n$, we propose the following estimator for $C_{kl}(\xi) = |\operatorname{corr}(\beta_k, \beta_l)|$.

$$\begin{aligned} C_{kl}^{est,n}(\xi) &:= \left| \widehat{\mathcal{A}}_{kl}^{est,n}(\xi) \right| / \sqrt{\left| \widehat{\mathcal{A}}_{kk}^{est,n}(\xi) \widehat{\mathcal{A}}_{ll}^{est,n}(\xi) \right|}, \quad \text{for all } \xi \in \mathbb{R}, \text{ where} \\ \mathcal{A}_{kl}^{est,n}(s) &:= \underline{Y}(s) - \tilde{\underline{R}}(s), \\ \underline{Y}(s) &:= \frac{1}{T+1} \sum_{t \in \{\tau\Delta\}_{\tau=0}^T} \left[\frac{1}{n} \sum_{\omega=1}^n \{Y_k(\omega; t - U(\omega)) Y_l(\omega; t + s - U(\omega))\} \right], \\ \tilde{\underline{R}}(s) &:= \frac{1}{T+1} \sum_{t \in \{\tau\Delta\}_{\tau=0}^T} \left[\frac{1}{n} \sum_{\omega=1}^n \{\tilde{R}_k(\omega; t - U(\omega)) \tilde{R}_l(\omega; t + s - U(\omega))\} \right]. \end{aligned} \tag{3.6}$$

The periodicity property of the Fourier transform implies that $C_{kl}^{est,n}(\xi)$ is a periodic function of ξ with period $1/\Delta$. Web Lemma B.1 implies that (3.6) is well-defined for all $\xi \in [0, 1/\Delta]$ except for at most

finitely many points ξ such that $\widehat{\mathcal{A}}_{kk}^{*est}(\xi)\widehat{\mathcal{A}}_{ll}^{*est}(\xi) = 0$.

$\mathcal{A}_{kl}^{est,n}(s)$ has a method of moments form except R_k in (3.2) is replaced with the estimated \tilde{R}_k . This has an effect on the consistency of $\mathcal{C}_{kl}^{est,n}(\xi)$ as an estimator for $\mathcal{C}_{kl}(\xi)$ and results in the asymptotic bias $|\lim_{n \rightarrow \infty} \mathcal{C}_{kl}^{est,n}(\xi) - \mathcal{C}_{kl}(\xi)|$. The bias can be small for properly chosen ξ . Specifically, we derive a formula of the bias as a function of ξ and choose ξ that minimizes the bias. Since $\tilde{R}_k(\omega; t)$ approximates $R_k(\omega; t)$, we model the difference $W_k(\omega; t) := R_k(\omega; t) - \tilde{R}_k(\omega; t)$ as random noise and assume that $\mathbf{W}(\omega; t) := (W_1(\omega; t), \dots, W_K(\omega; t))^T$ satisfies (i) $\mathbf{W}(\omega; t_1)$ is independent of $\mathbf{W}(\omega; t_2)$ if $t_1 \neq t_2$, (ii) $\mathbf{W}(\omega; t)$ is WSMZ, and (iii) $\Sigma_{kl} := \mathbb{E}[W_k(t)W_l(t)]$ for $t \in \mathcal{T}$. Because of $\Sigma_{kl} \leq \sqrt{\Sigma_{kk}\Sigma_{ll}}$ and $\mathbb{E}\beta_k = \mathbb{E}\beta_l = 0$, under the assumptions on $\mathbf{W}(\omega; t)$, Web Theorem B.2 implies

$$\lim_{n \rightarrow \infty} \mathcal{C}_{kl}^{est,n}(\xi) \approx \frac{\left| \mathbb{E}(\beta_k \beta_l) \frac{\widehat{h}_k(\xi) \widehat{h}_l(\xi)}{|\widehat{h}_k(\xi) \widehat{h}_l(\xi)|} e^{2\pi i \xi (t_{0,k} - t_{0,l})} \right|}{\sqrt{\mathbb{E}(\beta_k^2) \mathbb{E}(\beta_l^2)}} = \frac{|\mathbb{E}(\beta_k \beta_l)|}{\sqrt{\mathbb{E}(\beta_k^2) \mathbb{E}(\beta_l^2)}} = |\text{corr}(\beta_k, \beta_l)|$$

almost surely at frequencies ξ such that

$$\Sigma_{kk} / [(T+1)|\widehat{N}(\xi)\widehat{h}_k(\xi)|^2] \approx 0, \quad \Sigma_{ll} / [(T+1)|\widehat{N}(\xi)\widehat{h}_l(\xi)|^2] \approx 0. \quad (3.7)$$

The ξ resulting in sufficiently large $|\widehat{h}_k(\xi)|$ and $|\widehat{h}_l(\xi)|$ satisfying (3.7) reduces the estimation bias. From the signal processing perspective, large $|\widehat{h}_k(\xi)|$ and $|\widehat{h}_l(\xi)|$ filter out the random noise in $W_k(\omega; t)$, and HRFs act as band-pass filters (typically 0 – 0.15 Hz, Aguirre et al. (1997)). Hence, we are interested in $\xi \in (0, 0.15)$. Therefore, motivated by (3.7), $|\text{corr}(\beta_k, \beta_l)|$ is approximated by the median of $\mathcal{C}_{kl}^{est,n}(\xi)$ across $\xi \in (0, 0.15)$, since the median is more stable than mean. One typical curve of $\{\mathcal{C}_{kl}^{est,n}(\xi) | \xi \in \mathbb{R}\}$ is in Figure 1. The estimator $\mathcal{C}_{kl}^{est,n}(\xi)$ in (3.6) and the choice of ξ complete the estimation of $\mathcal{C}_{kl}(\xi) = |\text{corr}(\beta_k, \beta_l)|$. The estimation procedure is concluded in the ptFCE algorithm (Algorithm 1).

Algorithm 1 ptFCE Algorithm

Input: (i) Task-fMRI BOLD signals $\{(Y_k(\omega; \tau\Delta), Y_l(\omega; \tau\Delta))\}_{\tau=0}^T$ for sampled subjects $\omega \in \{1, \dots, n\}$; (ii) repetition time Δ ; (iii) the stimulus signal $\{N(\tau\Delta)\}_{\tau=0}^T$; (iv) latency $t_{0,k'} = \tau_{0,k'}\Delta$ with some $\tau_{0,k'} \in \mathbb{Z}$ for $k' \in \{k, l\}$, and their default values are $t_{0,k'} = 0$ for $k' \in \{k, l\}$; (v) HRF $h_{k'}$ for $k' \in \{k, l\}$. The default HRFs are $h_k = h_l =$ the R function `canonicalHRF` with its default parameters.

Output: An estimation of the ptFC $|\text{corr}(\beta_k, \beta_l)|$ between the k^{th} and l^{th} nodes.

- 1: Generate i.i.d. $\{U(\omega)\}_{\omega=1}^n$ from the uniform distribution on $\mathcal{T} = \{\tau\Delta\}_{\tau=0}^T$.
 - 2: For each $\omega \in \{1, \dots, n\}$ and $k' \in \{k, l\}$, apply the AMUSE algorithm to input (3.5) and obtain estimated reference signals $\{\tilde{R}_{k'}(\omega; \tau\Delta)\}_{\tau=0}^T$.
 - 3: Compute the estimator $\mathcal{C}_{kl}^{est,n}(\xi)$ in (3.6) and the median of $\{\mathcal{C}_{kl}^{est,n}(\xi) | \xi \in (0, 0.15)\}$. The median is the output of this algorithm.
-

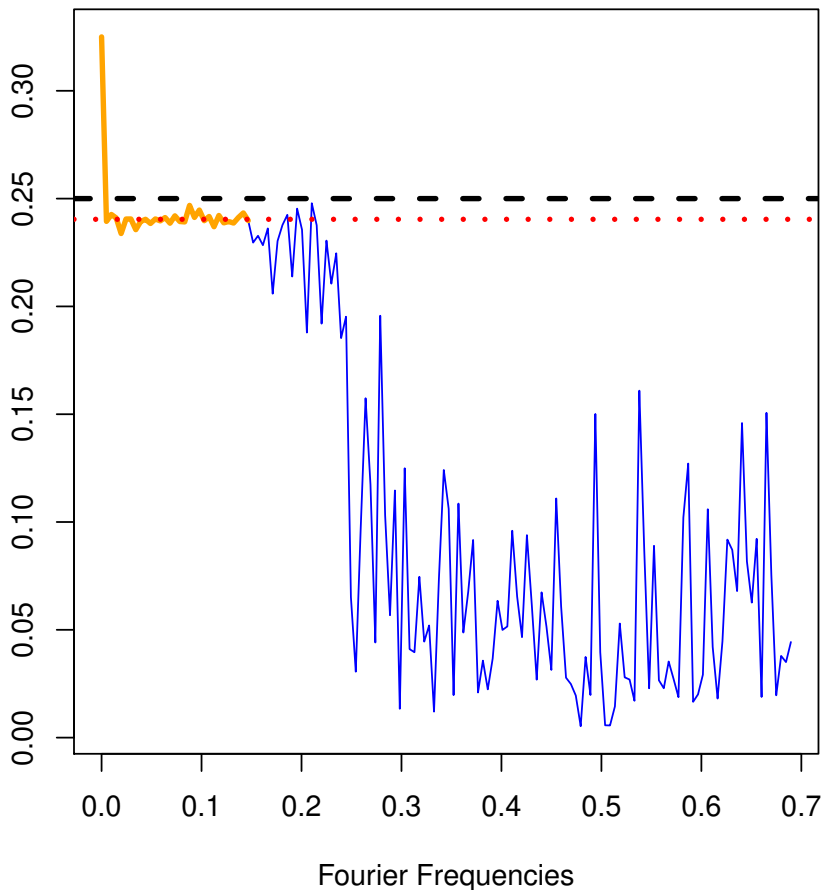


Figure 1: To generate this figure, we first generate synthetic BOLD signals using the Mechanism 0 in Appendix E with sample size $n = 308$ and underlying $\rho = 0.25$ (presented by the black dashed line). Then we apply our proposed ptFCE algorithm to the synthetic BOLD signals generated by Mechanism 0. The solid blue curve presents the estimator $C_{kl}^{est,n}(\xi)$ as a function of Fourier frequencies $\xi \in (0, \frac{1}{2\Delta})$, and the solid orange curve presents $\{C_{kl}^{est,n}(\xi) | \xi \in (0, 0.15)\}$ for taking the desired median. The unreasonably large value part of this orange curve motivates us to implement the median instead of the mean of $\{C_{kl}^{est,n}(\xi) | \xi \in (0, 0.15)\}$. The dotted red line presents the median of $C_{kl}^{est,n}(\xi)$ across $\xi \in (0, 0.15)$, i.e., the output of the ptFCE algorithm for the synthetic BOLD signals.

4 Simulations

When comparing methods for FC estimation, direct comparisons of methods are difficult as the estimates are defined on different scales (Cisler et al. (2014)). In the context of FC analysis, we may compare the methods by measuring their accuracy in correctly identifying the relative values of FC among pairs of nodes estimated by each approach, i.e., the performance of the algorithm in terms of detecting underlying “weak vs. strong” patterns instead of the estimated values. Specifically, suppose we investigate two pairs of nodes. The connectivity between one pair is weak while the connectivity between another pair is strong; we are interested in whether the estimated value for the weak connectivity is smaller than that of the strong connectivity. Therefore, in this section, we only compare ptFCE with other approaches in

detecting underlying “weak vs. strong” patterns. Simulation studies showing the performance of ptFCE in terms of estimation bias and variance are presented in Appendix D. For the comparative analysis, we use synthetic data generated by two different mechanisms designed to mimic the properties of HCP motor data. We design the simulations by using non-canonical HRFs in generating synthetic data to illustrate the robustness of our algorithm that uses the canonical HRF as input. We show that the algorithm can still detect underlying task-evoked FC patterns.

We compare the ptFCE algorithm with the following methods: beta-series regression, *naive Pearson correlation*, *task Pearson correlation*, coherence analysis using two data-generating mechanisms such that the first is based on model (2.2) for defining ptFCs, while the second is motivated by Pearson correlations. We use the second data generating mechanism to illustrate the comparable performance of our proposed approach with others even when the data generating mechanism is not compatible with the ptFC framework.

Mechanism 1: Step 1, generate coefficients $(\beta_1(\omega), \beta_2(\omega), \beta_3(\omega))^T \sim N_3(\mathbf{0}, (\sigma_{ij})_{1 \leq i, j \leq 3})$ for $\omega = 1, \dots, n$. Assume $\rho_{ij} := |\sigma_{ij} / \sqrt{\sigma_{ii}\sigma_{jj}}|$, for $(i, j) \in \{(1, 2), (2, 3)\}$ are the true underlying ptFCs between nodes 1 and 2 and between nodes 2 and 3, respectively. **Step 2**, generate reference signals $\{R_{k'}(\omega; \tau\Delta) = Q_{k'}(\omega; \tau\Delta) + \epsilon_{k'}(\omega; \tau\Delta)\}_{\tau=0}^T$, for all ω and $k' \in \{1, 2, 3\}$, where the $3nT$ noise values $\{\epsilon_{k'}(\omega; \tau\Delta) | k' = 1, 2, 3; \omega = 1, \dots, n; \tau = 0, \dots, T\} \sim_{iid} N(0, V)$. **Step 3**, compute synthetic BOLD signals $\{Y_{k'}(\omega; \tau\Delta) | k' = 1, 2, 3\}_{\tau=0}^T$, for $\omega = 1, \dots, n$, by $Y_{k'}(\omega; \tau\Delta) = 9000 + \beta_{k'}(\omega) \times (N * h_{k'}) (\tau\Delta) + R_{k'}(\omega; \tau\Delta)$. $\mathbf{Y}(\omega; t) := \{Y_{k'}(\omega; \tau\Delta)\}_{k'=1}^3$.

Mechanism 2: Step 1, for each $\omega \in \{1, \dots, n\}$, generate independent normal vectors

$$\{\boldsymbol{\varepsilon}(\omega; \tau\Delta) = (\varepsilon_1(\omega; \tau\Delta), \varepsilon_2(\omega; \tau\Delta), \varepsilon_3(\omega; \tau\Delta))^T\}_{\tau=0}^T,$$

where $\boldsymbol{\varepsilon}(\omega; \tau\Delta) \sim N_3(\mathbf{0}, \boldsymbol{\Sigma}_{task})$ if $N(\tau\Delta) = 1$, and $\boldsymbol{\varepsilon}(\omega; \tau\Delta) \sim N_3(\mathbf{0}, \boldsymbol{\Sigma}_{resting})$ if $N(\tau\Delta) = 0$; matrices $\boldsymbol{\Sigma}_{task}$ and $\boldsymbol{\Sigma}_{resting}$ share the same diagonals, the off-diagonal elements of $\boldsymbol{\Sigma}_{resting}$ are 0, and $\{\varrho_{ij}\}_{i,j=1}^3$ denote the correlations deduced from covariance matrix $\boldsymbol{\Sigma}_{task}$. **Step 2**, compute $Y_{k'}(\omega; \tau\Delta) = N * h_{k'}(\tau\Delta) + \sum_{j=1}^4 N_j * h_{k',j}(\tau\Delta) + \varepsilon_{k'}(\tau\Delta)$, for $k' \in \{1, 2, 3\}$, where the tasks $\{N_j(t)\}_{j=1}^4$ are nuisance tasks, and $\{h_{k',j}(t)\}_{j=1}^4$ are the corresponding HRFs. **Step 3**, repeat Steps 1 and 2 for all $\omega = 1, \dots, n$.

Details of Mechanisms 1 and 2 are in Appendix E. In Mechanism 2, the zero off-diagonal elements of $\boldsymbol{\Sigma}_{resting}$ indicate no task-evoked connectivity when the task of interest is absent. When $N(\tau\Delta) = 1$, the correlation ϱ_{ij} in $\boldsymbol{\Sigma}_{task}$ measures the connectivity between nodes i and j evoked by task $N(\tau\Delta) = 1$.

We are interested in estimating the connectivity between nodes 1, 2 and nodes 2, 3. With the synthetic signals $\{\mathbf{Y}(\omega; t)\}_{\omega=1}^n$ generated by Mechanisms 1 or 2, the existing methods are implemented as follows.

Naive Pearson correlation: For each subject ω and underlying ρ_{ij} or ϱ_{ij} , compute the Pearson correlation between $\{Y_i(\omega; \tau\Delta)\}_{\tau=0}^T$ and $\{Y_j(\omega; \tau\Delta)\}_{\tau=0}^T$ across all τ and denote the absolute value of this correlation by $\hat{\rho}_{ij,\omega}^{naiveCorr}$. Let $\hat{\rho}_{ij,\omega}^{naiveCorr}$ and $\hat{\rho}_{ij,\omega}^{naiveCorr}$ denote the mean and median, respectively, of $\{\hat{\rho}_{ij,\omega}^{naiveCorr}\}_{\omega=1}^n$ across all ω .

Task Pearson correlation: For each ω and underlying ρ_{ij} or ϱ_{ij} , compute the Pearson correlation between $\{Y_i(\omega; \tau\Delta)|N(\tau\Delta) = 1\}$ and $\{Y_j(\omega; \tau\Delta)|N(\tau\Delta) = 1\}$ across τ such that $N(\tau\Delta) = 1$ and denote its absolute value by $\hat{\rho}_{ij,\omega}^{taskCorr}$. Compute the mean and median of $\{\hat{\rho}_{ij,\omega}^{taskCorr}\}_{\omega=1}^n$ across ω and denote them by $\hat{\rho}_{ij,\omega}^{taskCorr}$ and $\hat{\rho}_{ij,\omega}^{taskCorr}$, respectively.

Details of implementing the beta-series regression and coherence analysis to obtain estimates $(\hat{\rho}_{ij,\omega}^{betaS}, \hat{\rho}_{ij,\omega}^{betaS})$ and $(\hat{\rho}_{ij,\omega}^{Coh}, \hat{\rho}_{ij,\omega}^{Coh})$ are presented in Appendix G.

Let $(\rho_{12}, \rho_{23}) = (\varrho_{12}, \varrho_{23}) = (0.4, 0.6)$, indicating weak (0.4) or strong (0.6) connectivity between the two node pairs. We use sample sizes $n = 50$ and 308 to illustrate the performance in different sample sizes, where 308 is the size of the HCP data set. PtFCs estimated by the ptFCE algorithm are denoted by $(\hat{\rho}_{12}, \hat{\rho}_{23})$. For each simulated data set, applying all FC estimation methods, we obtain estimates $\{(\hat{\rho}_{ij}, \hat{\rho}_{ij,\omega}^{betaS}, \dots, \hat{\rho}_{ij,\omega}^{Coh})|i < j\}_{i,j=1}^3$. For each method, we evaluate whether it can identify the “weak vs. strong” pattern. For example, our proposed ptFCE algorithm is effective if $\hat{\rho}_{12} < \hat{\rho}_{23}$. We repeat this procedure 500 times. The rates of correct identification of the connectivity patterns across 500 simulations are presented in Table 1. When synthetic BOLD signals are from the mechanism compatible with the definition of ptFCs - Mechanism 1, our ptFCE algorithm performs overwhelmingly better than other methods. If the synthetic signals are from the mechanism motivated by Pearson correlations - Mechanism 2, our proposed algorithm still provides a good identification rate and is better than the coherence analysis. Importantly, it is unlikely that the true data generating process in task-fMRI follows the second data generating process. Mechanism 2 implies the effect of task disappears as soon as the task is absent. However, it is known that there is a delay in brain response associated with time needed by brain vasculature to respond to the decrease in oxygen (Lindquist et al. (2008)). Even in this unrealistic scenario, our proposed method is comparable with others. Naive Pearson correlation and coherence analysis are designed to measure FC evoked by both the task of interest and nuisance tasks. In contrast, beta-series regression, task Pearson correlations, and ptFCE are developed for quantifying FC evoked by specific tasks of interest. Hence, only beta-series regression, task Pearson correlations, and

Table 1: Identification rates $\hat{p} := n'/n$ of different methods for the “weak vs strong” pattern, where n' is the number of correct identifications among all $n = 500$ synthetic samples. The correct identification rates in the table are presented in 95%-confidence interval form $\hat{p} \pm z_{0.975} \cdot \sqrt{\hat{p}(1 - \hat{p})/n}$, where $z_{0.975} \approx 1.96$ is the 0.975-quantile of the standard normal distribution $N(0, 1)$.

Methods	Rates ($n = 50$)		Rates ($n = 308$)	
	Mech. 1	Mech. 2	Mech. 1	Mech. 2
ptFCE	82.8(± 10.5)%	67.4(± 13.0)%	99.8(± 0.5)%	88.4(± 2.9)%
SLR	66.4(± 13.1)%	56.8(± 13.7)%	84.8(± 3.6)%	63.4(± 5.4)%
naive Pearson (mean)	58.2(± 13.7)%	93.8(± 6.7)%	69.0(± 5.2)%	100(± 0)%
naive Pearson (median)	55.6(± 13.8)%	88.0(± 9.0)%	62.2(± 5.4)%	100(± 0)%
task Pearson (mean)	47.6(± 13.8)%	100(± 0)%	48.6(± 5.6)%	100(± 0)%
task Pearson (median)	47.8(± 13.8)%	100(± 0)%	50.6(± 5.6)%	100(± 0)%
beta-series (mean)	49.4(± 13.9)%	96.6(± 5.0)%	48.8(± 5.6)%	100(± 0)%
beta-series (median)	48.2(± 13.9)%	97.8(± 4.1)%	47.6(± 5.6)%	100(± 0)%
coherence (mean)	51.0(± 13.9)%	55.8(± 13.8)%	60.8(± 5.5)%	72.0(± 5.0)%
coherence (median)	51.6(± 13.6)%	57.6(± 13.7)%	58.8(± 5.5)%	68.0(± 5.2)%

ptFCE algorithms are useful when estimating task-evoked FC. Additionally, task Pearson correlation model assumes that the effect of task of interest disappears immediately when the task is absent. Hence, because of the delay in brain response, task Pearson correlations may be biased. Lastly, Table 1 shows that ptFCE performs better than the beta-series regression for data from Mechanism 1. In addition, we compare the SLR approach introduced in the beginning of Section 3 with the ptFCE algorithm. When the synthetic data are generated from Mechanism 1, although SLR performs overwhelmingly better than the existing methods, it is inferior to the ptFCE algorithm. When the synthetic data are generated from Mechanism 2, which violates the assumptions in model (2.2), SLR is hardly better than a random guess.

PtFCE is computationally efficient and scalable. On a PC with 2.4 GHz 8-Core Intel Core i9 processor, the approximate computational time of ptFCE is 3.5 seconds for 50 subjects and 11.5 seconds for 1000 subjects.

5 Analysis of HCP Motor Data

In this section, we present estimation of FC in a task-evoked functional MRI study using data from HCP. For comparison, we apply the ptFCE algorithm and existing methods to measure FC in the database of 308 subjects from HCP performing motor tasks. A detailed description of the HCP data is provided in Section 1. We model squeezing right toes as the task of interest. Before the estimation step, we compute region-specific time courses using the AAL atlas (Tzourio-Mazoyer et al. (2002)) that consists of 120 brain regions. For each region, we extract the voxel-specific time series in that region and compute their

spatial average for each time point. As a result, we obtain 120 time courses corresponding to 120 regions of interest. We select the left precentral gyrus (PreCG.L) as the seed region since it is located in the primary motor cortex and the motions of the right toes are associated with the left brain. We measure FC induced by $N(t)$ at a population level between the seed region and other regions using the following five approaches: the ptFCE algorithm, naive and task Pearson correlations, beta-series regression, and coherence analysis. In Section 4, the means $\hat{\rho}_{ij,mean}^{naiveCorr}$, $\hat{\rho}_{ij,mean}^{taskCorr}$, $\hat{\rho}_{ij,mean}^{betaS}$, and $\hat{\rho}_{ij,mean}^{Coh}$ tend to perform better than the corresponding medians. Hence, we show only the mean results in data analysis. Because of numerical issues, we omit regions CB7.L, CB7.R, and CB10.L and investigate the rest of the 117 regions. The detailed procedures of applying these approaches are described in Section 4.

Suppose $\mathcal{X}_{r,j}$, for $r = 1, \dots, 116$ and $j = 1, \dots, 5$, are the estimated FC values between PreCG.L and other 116 regions computed using the referred five approaches indexed by j . Since these approaches use different scales, we standardize the estimates by $\mathcal{X}_{r,j}^{(st)} = \frac{\mathcal{X}_{r,j} - \min\{\mathcal{X}_{r',j}\}_{r'=1}^{116}}{\max\{\mathcal{X}_{r',j}\}_{r'=1}^{116} - \min\{\mathcal{X}_{r',j}\}_{r'=1}^{116}}$, for all r and j , to enable comparisons. The standardized versions of the estimates are presented in Figure 2. To quantify the agreement between estimation approaches implemented in this study, we use 0.5 as the threshold for standardized $\mathcal{X}_{r,j}^{(st)}$ to determine whether the node r is connected to PreCG.L according to method j . Specifically, if $\mathcal{X}_{r,j}^{(st)} > 0.5$, then method j estimates that region r is functionally connected to PreCG.L. Define $\mathbf{1}(\mathcal{X}_{r,j}^{(st)} > 0.5) =: \vartheta_{r,j}$. As a result of applying each method j , we obtain the connectivity pattern $\{\vartheta_{r,j}\}_{r=1}^{116}$. Agreement between methods j_1 and j_2 , for all $j_1, j_2 = 1, \dots, 5$, is measured by Cohen's kappa statistic denoted as κ_{j_1, j_2} (Cohen (1960)) using classification results $\{\vartheta_{r, j_1}\}_{r=1}^{116}$ and $\{\vartheta_{r, j_2}\}_{r=1}^{116}$. The κ_{j_1, j_2} along with p-values testing the null hypothesis indicating that the extent of agreement between each pair of methods is the same as random ($\kappa_{j_1, j_2} = 0$) are presented in Table 2. Using $\alpha = 0.05$ and implementing multiple comparisons correction, we find that all methods have significant agreement with each other.

The postcentral gyrus (PoCG.L) region is identified by all five methods as the region with strongest functional connectivity with the seed region. The estimated ptFCs indicate that the neuronal activity of the left precentral gyrus and that of left postcentral gyrus corresponding to squeezing right toes are highly correlated (either negatively or positively). Magnitudes of the neuronal activity corresponding to the task of interest in these two regions tend to be linearly dependent across the entire population. In addition to modeling advantages of our proposed ptFC approach described in Section 2.2, we obtain differences between the estimates of ptFCE and those of competitor methods. We identify high connectivity between several regions and the seed region that are missed by competitor methods. Specifically, we obtain high task-evoked FC between the seed region and left/right thalamus (passing motor signals to the cerebral

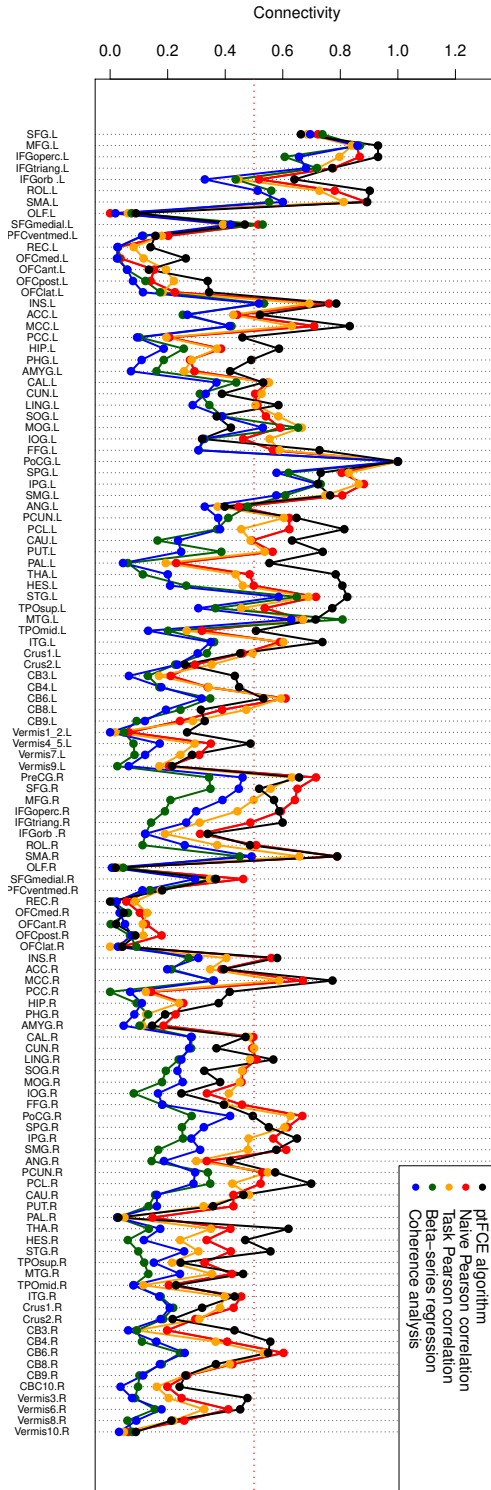


Figure 2: Illustration of estimation results from five FC estimation methods. The horizontal axis indicates the 116 regions compared to PreCG.L. The abbreviations of region names are provided in the data set `aa12.120` in the R package `brainGraph`. The vertical axis presents the standardized connectivity measurements $\mathcal{X}_{r,j}^{(st)}$ between each region and the seed region PreCG.R. The red dotted horizontal line indicates the threshold 0.5 implemented for determining the connected/nonconnected relationships between PreCG.L and other regions.

Table 2: The Kappa statistics between each pair of methods are computed using the R function `Kappa.test` in package `fmsb`. The p-value of a Kappa statistic is presented in the parentheses below the statistic.

Methods	ptFCE	naive Persn	task Persn	beta series	coherence
ptFCE	*	0.696 (< 0.0001)	0.503 (< 0.0001)	0.260 (0.00636)	0.277 (0.00402)
naive Persn	*	*	0.732 (< 0.0001)	0.391 (0.00022)	0.367 (0.00051)
task Persn	*	*	*	0.478 (< 0.0001)	0.497 (< 0.0001)
beta series	*	*	*	*	0.961 (< 0.0001)
coherence	*	*	*	*	*

6 Conclusions

In this paper, we propose a rigorous random-effects type model for task-evoked BOLD signals in fMRI studies. Based on this model, we define a measurement, ptFC, of task-evoked FC at a population level. We discuss shortcomings of several existing methods for evaluating task-evoked population-level FC that are addressed by our proposed framework. Thorough theoretical results on the properties of our proposed estimation procedure are presented. We develop the ptFCE algorithm for estimating ptFC and show that it is computationally efficient. The superior performance of our proposed ptFCE algorithm when data are generated using a block-design task fMRI data-generating mechanism is illustrated using simulation studies. We use ptFCE to estimate ptFCs in a motor-task data set publicly available from HCP. PtFCE results in similar FC patterns with the widely used existing methods. Additionally, ptFCE provides FC discoveries of connections between nodes not identified by existing methods. Extensions of our proposed work can include development of a subject-level task-evoked FC definition and estimation procedure, as well as considerations on the inclusion of interaction terms $P_k(\omega; t)Q_k(\omega; t)$ (see Appendix H).

Data Availability Statement

The data supporting the findings in Section 5 are publicly available on the HCP website:

<https://protocols.humanconnectome.org/HCP/3T/task-fMRI-protocol-details.html> (Barch et al. (2013)).

The R code for simulation studies and data analyses is available at

<https://github.com/KMengBrown/Population-level-Task-evoked-Functional-Connectivity.git>.

Appendix

A Relationship between the proposed BOLD signal model and some existing models

In this paper, we implement the following model for observed task-fMRI BOLD signals $Y_k(\omega; t)$, for $\omega \in \Omega$ and $k \in \{1, \dots, K\}$.

$$\begin{aligned} Y_k(\omega; t) &= P_k(\omega; t) + Q_k(\omega; t) + \epsilon_k(\omega; t), \quad \text{with} \\ P_k(\omega; t) &= \beta_k(\omega) \times N * h_k(t - t_{0,k}), \end{aligned} \tag{A.1}$$

where $P_k(\omega; t)$ denotes the BOLD signal component stemming solely from the task $N(t)$ of interest, $Q_k(\omega; t)$ denotes spontaneous neuronal activity component and neuronal activity responding to nuisance tasks, and $\epsilon_k(\omega; t)$ is random error. Additionally, $t_{0,k}$ denotes the population shared latency and is usually smaller than the experimental unit, e.g., see [Zhang et al. \(2013\)](#) (p 138). The HRF shared by the whole population is $h_k(t)$. Here, we explore three existing models for BOLD signals. We show that these models are special cases of our proposed BOLD signal model (A.1).

Example 1: Using the notations in our paper, the BOLD signal model implemented by [Zhang et al. \(2013\)](#) can be represented as follows.

$$Y_k(\omega; t) = X_k(\omega; t)^T d(\omega) + \sum_{\gamma=1}^{\Gamma} \beta_{k,\gamma}(\omega) \times (N_\gamma * h_{k,\gamma})(t) + \epsilon_k(\omega; t), \tag{A.2}$$

where $N_\gamma(t)$ are task stimulus signals, $h_{k,\gamma}(t)$ are corresponding HRFs, and $X_k(\omega; t)^T d(\omega)$ characterizes the BOLD signal components stemming from other known sources, e.g., respiration and heartbeat. The BOLD signal model proposed by [Zhang et al. \(2013\)](#) includes participant-dependent latency times. These latency times are essentially modeled as zero, since the values are usually much smaller than the corresponding experimental time unit.

Suppose we are interested in the first experimental task $N_1(t)$. Define the following.

$$\begin{aligned} \beta_k(\omega) &:= \beta_{k,1}(\omega), \quad N(t) := N_1(t), \quad P_k(\omega; t) = \beta_k(\omega) \times (N * h_k)(t), \\ Q_k(\omega; t) &:= X_k(\omega; t)^T d(\omega) + \sum_{\gamma=2}^{\Gamma} \beta_{k,\gamma}(\omega) \times (N_\gamma * h_{k,\gamma})(t). \end{aligned} \tag{A.3}$$

Then (A.2) is equivalent to the model (A.1) with latency $t_{0,k} = 0$, and there is no interaction term $P_k(\omega; t)Q_k(\omega; t)$.

Example 2: Using the notations in our paper, the BOLD signal model implemented by Warnick et al. (2018) is represented as follows (see the equations (1) and (2) in Warnick et al. (2018)).

$$Y_k(\omega; t) = \mu_k(\omega) + \sum_{\gamma=1}^{\Gamma} \beta_{k,\gamma}(\omega) \times (N_\gamma * h_{k,\gamma})(t) + \epsilon_k(\omega; t), \quad (\text{A.4})$$

where $N_\gamma(t)$ are task stimulus signals, $h_{k,\gamma}(t)$ are corresponding HRFs, $\epsilon_k(\omega; t)$ are random error, and $\mu_k(\omega)$ present the baseline. Suppose we are interested in task $N_1(t)$. We apply the transform (A.3) and define $Q_k(\omega; t) = \mu_k(\omega) + \sum_{\gamma=2}^{\Gamma} \beta_{k,\gamma}(\omega) \times (N_\gamma * h_{k,\gamma})(t)$. Then model (A.4) is equivalent to our proposed model (A.1) with latency $t_{0,k} = 0$, without an interaction term $P_k(\omega; t)Q_k(\omega; t)$.

Example 3: Motivated by the *independent component analysis* framework, Joel et al. (2011) implemented the following model for task-fMRI BOLD signals.

$$\begin{aligned} Y_k(\omega; t) = & M_{m,k}(\omega) \{ \beta_{tm}(\omega) \times N * h_k(t) + \beta_{im}(\omega) \iota_m(t) \} \\ & + M_{v,k}(\omega) \{ \beta_{tv}(\omega) \times N * h_k(t) + \beta_{iv}(\omega) \iota_v(t) \} \\ & + M_b(\omega) \beta_b(\omega) \gamma(\omega; t), \end{aligned} \quad (\text{A.5})$$

where $M_{(\cdot),k}$ is the spatial mask at the k^{th} node for visual cortex ($M_{v,k}$), motor cortex ($M_{m,k}$) or the whole brain (M_b), $N(t)$ is stimulus signal corresponding to the task of interest, $h_k(t)$ is an HRF, $\iota_{(\cdot)}$ is the intrinsic activity of the corresponding cortex, $\gamma(\omega; t)$ presents random noise, and $\beta_{tm}(\omega)$, $\beta_{im}(\omega)$, $\beta_{tv}(\omega)$, $\beta_{iv}(\omega)$, $\beta_b(\omega)$ are the weights of motor task, intrinsic motor activity, visual task, intrinsic visual activity and noise, respectively.

Since the task of interest in the HCP data is a motor task, we define the following notations.

$$\begin{aligned} \beta_k(\omega) & := M_{m,k}(\omega) \times \beta_{tm}(\omega), \\ Q_k(\omega) & := M_{m,k}(\omega) \beta_{im}(\omega) \iota_m(t) + M_{v,k}(\omega) \{ \beta_{tv}(\omega) \times N * h_k(t) + \beta_{iv}(\omega) \iota_v(t) \}, \\ \epsilon_k(\omega; t) & = M_b(\omega) \beta_b(\omega) \gamma(\omega; t). \end{aligned}$$

Using the notations above, model (A.5) is the same as model (A.1) with latency $t_{0,k} = 0$, and there is no interaction term $P_k(\omega; t)Q_k(\omega; t)$.

B Lemmas, Theorems, and Their Proofs

In this section, we provide proofs of theorems and lemmas presented in our paper. Throughout this section, the time index collection \mathcal{T} denotes $\{\tau\Delta\}_{\tau=0}^T$, and Ω is a discrete and finite set.

Lemma B.1. *If $f : \mathcal{T} \rightarrow \mathbb{R}$ is not constant zero, its Fourier transform $\widehat{f}(\xi)$ has at most finitely many zero points - $\xi \in \mathbb{R}$ such that $\widehat{f}(\xi) = 0$ - in any compact subset of \mathbb{R} .*

Proof. Define the complex function $\Phi_f(z) := \frac{1}{T+1} \sum_{\tau=0}^T f(\tau\Delta)e^{-2\pi z(\tau\Delta)}$, for all $z = \eta + i\xi \in \mathbb{C}$. Since it is straightforward that $\Phi_f(z)$ satisfies the *Cauchy-Riemann* equation $\frac{\partial}{\partial \bar{z}}\Phi_f(z) = 0$, where $\frac{\partial}{\partial \bar{z}} = \frac{1}{2}(\frac{\partial}{\partial \eta} + i\frac{\partial}{\partial \xi})$ is a Wirtinger derivative, the Looman–Menchoff theorem implies that $\Phi_f(z)$ is a holomorphic function. Then the zero points of $\Phi_f(z)$ are isolated, i.e., every zero point has a neighbourhood that does not contain any other zero point (Theorem 3.7 of [Conway \(1973\)](#)). Therefore, $\widehat{f}(\xi) = \Phi_f(i\xi)$ implies the desired result. \square

Theorem B.1. *Suppose signals $\{Y_k(\omega; t) | t \in \mathcal{T}\}_{k=1}^K$, for $\omega \in \Omega$, are defined as in (A.1), $\mathbb{E}\beta_k = \mathbb{E}R_k(t) = 0$, and $t_{0,k} = \tau_{0,k}\Delta$ with some $\tau_{0,k} \in \mathbb{Z}$ for all $k = 1, 2, \dots, K$ and $t \in \mathcal{T}$. Let the random variable $U : \Omega \rightarrow \mathcal{T}$ be uniformly distributed on \mathcal{T} . Furthermore, we assume that $U(\omega)$, $\{\beta_k(\omega)\}_{k=1}^K$, and $\{R_k(\omega; t) | t \in \mathcal{T}\}_{k=1}^K$ are independent. Then, the autocovariance differences $\mathcal{A}_{kl}(s) := \mathbb{E}\{Y_k(t-U)Y_l(t+s-U)\} - \mathbb{E}\{R_k(t-U)R_l(t+s-U)\}$ depend only on s , the Fourier transforms of $\mathcal{A}(s)$ are*

$$\widehat{\mathcal{A}}_{kl}(\xi) = \mathbb{E}(\beta_k\beta_l) \times \left| \widehat{N}(\xi) \right|^2 \overline{\widehat{h}_k(\xi)} \widehat{h}_l(\xi) e^{2\pi i(t_{0,k} - t_{0,l})\xi}.$$

Furthermore, we have the following representation.

$$\mathcal{C}_{kl}(\xi) := |\widehat{\mathcal{A}}_{kl}(\xi)| / \sqrt{|\widehat{\mathcal{A}}_{kk}(\xi)\widehat{\mathcal{A}}_{ll}(\xi)|} = |\text{corr}(\beta_k, \beta_l)|, \text{ for all } \xi \in \mathbb{R}.$$

Proof. The independence between $U(\omega)$, $\{\beta_k(\omega)\}_{k=1}^K$, and $\{R_k(\omega; t) | t \in \mathcal{T}\}_{k=1}^K$ implies

$$\begin{aligned}
& \mathbb{E}[Y_k(t - U)Y_l(t + s - U)] - \mathbb{E}[R_k(t - U)R_l(t + s - U)] \\
&= \mathbb{E}(\beta_k\beta_l) \times \mathbb{E}[(N * h_k)(t - t_{0,k} - U) \times (N * h_l)(t + s - t_{0,l} - U)] \\
&= \mathbb{E}(\beta_k\beta_l) \times \frac{1}{T+1} \sum_{u=0}^T \left\{ (N * h_k)((\tau - \tau_{0,k} - u)\Delta) \times (N * h_l)((\underline{s} + \tau_{0,k} - \tau_{0,l})\Delta + (\tau - \tau_{0,k} - u)\Delta) \right\} \\
&= \mathbb{E}(\beta_k\beta_l) \times \frac{1}{T+1} \sum_{v=-(\tau-\tau_{0,k})}^{T-(\tau-\tau_{0,k})} \left\{ (N * h_k)(-v\Delta) \times (N * h_l)((\underline{s} + \tau_{0,k} - \tau_{0,l})\Delta - v\Delta) \right\} \\
&= \mathbb{E}(\beta_k\beta_l) \times [N * h_k(-\cdot)] * [N * h_l](s + (t_{0,k} - t_{0,l})), \tag{B.1}
\end{aligned}$$

which only depends on s and does not depend on t . Here, the last equality follows from the periodic extension and the definition of convolution. Then, we have the following Fourier transform,

$$\begin{aligned}
\widehat{A}_{kl}(\xi) &= \mathbb{E}(\beta_k\beta_l) \times \overline{\widehat{(N * h_k)}(\xi)} \widehat{(N * h_l)}(\xi) e^{2\pi i(t_{0,k} - t_{0,l})\xi} \\
&= \mathbb{E}(\beta_k\beta_l) \times \left| \widehat{N}(\xi) \right|^2 \overline{\widehat{h_k}(\xi)} \widehat{h_l}(\xi) e^{2\pi i(t_{0,k} - t_{0,l})\xi},
\end{aligned}$$

for all $\xi \in \mathbb{R}$, which implies $\mathcal{C}_{kl}(\xi) = |\text{corr}(\beta_k, \beta_l)|$ for all $\xi \in \mathbb{R}$. \square

Lemma B.2. *The vector-valued stochastic process $\mathbf{Z}(\omega; t) = \{(Z_1(\omega; t), Z_2(\omega; t), \dots, Z_K(\omega; t))^T\}_{t \in \mathcal{T}}$ is defined on probability space $(\Omega, 2^\Omega, \mathbb{P})$ and is weakly stationary with mean zero, $U : \Omega \rightarrow \mathcal{T}$ is uniformly distributed, and $U(\omega)$ and $\mathbf{Z}(\omega; t)$ are independent. Then the vector-valued stochastic process $\mathbf{Z}(\omega; t - U(\omega)) = \{(Z_1(\omega; t - U(\omega)), Z_2(\omega; t - U(\omega)), \dots, Z_K(\omega; t - U(\omega)))^T\}_{t \in \mathcal{T}}$ is weakly stationary with mean zero as well. Additionally, $\mathbb{E}[Z_k(t - U)Z_l(t + s - U)] = \mathbb{E}[Z_k(0)Z_l(s)]$, for all $k, l = 1, 2, \dots, K$.*

Proof. Let μ be the probability measure on \mathcal{T} associated with the uniform random variable $U : \Omega \rightarrow \mathcal{T}$, i.e., $\mu = \mathbb{P} \circ U^{-1}$, then we have $\mathbb{E}\{Z_k(t - U)\} = \int_{\mathcal{T}} \mathbb{E}\{Z_k(t - U) | U = u\} \mu(du)$. The independence between U and \mathbf{Z} implies $\mathbb{E}\{Z_k(t - U) | U = u\} = \mathbb{E}\{Z_k(t - u)\} = 0$ for all t , which results in $\mathbb{E}\{Z_k(t - U)\} = 0$

for all $t \in \mathcal{T}$. Similarly, we have

$$\begin{aligned}
\mathbb{E} \{Z_k(t-U)Z_l(t+s-U)\} &= \int_{\mathcal{T}} \mathbb{E} \{Z_k(t-U)Z_l(t+s-U)|U=u\} \mu(du) \\
&= \int_{\mathcal{T}} \mathbb{E} \{Z_k(t-u)Z_l(t+s-u)\} \mu(du) \\
&= \int_{\mathcal{T}} \mathbb{E} \{Z_k(0)Z_l(s)\} \mu(du) \\
&= \mathbb{E} \{Z_k(0)Z_l(s)\},
\end{aligned}$$

This completes the proof of the desired result. \square

Theorem B.2. *Suppose we have the following random vectors and stochastic processes.*

- $\mathfrak{B} := \{(\beta_k(\omega), \beta_l(\omega))\}_{\omega}^n$ are n i.i.d. random vectors.
- $\mathfrak{R} := \left\{ \left(\tilde{R}_k(\omega; t), \tilde{R}_l(\omega; t) \right) \mid t \in \mathcal{T} \right\}_{\omega=1}^n$ are n i.i.d. stochastic processes.
- $\mathfrak{W} := \{(W_k(\omega; t), W_l(\omega; t)) \mid t \in \mathcal{T}\}_{\omega=1}^n$ are n i.i.d. stochastic processes satisfying (i) random vectors $(W_k(\omega; t_1), W_l(\omega; t_1))$ and $(W_k(\omega; t_2), W_l(\omega; t_2))$ are independent whenever $t_1 \neq t_2$, (ii) the stochastic process $\{(W_k(\omega; t), W_l(\omega; t)) \mid t \in \mathcal{T}\}$ is weakly stationary with mean zero, and (iii) $\Sigma_{kl} = \mathbb{E} \{W_k(t)W_l(t)\}$ for all $t \in \mathcal{T}$.

The collections $\mathfrak{B}, \mathfrak{R}, \mathfrak{W}$ are independent. Furthermore, we have the following task-fMRI BOLD signals.[†]

$$Y_{k'}(\omega; t) = \beta_{k'}(\omega) \times N * h_{k'}(t - t_{0,k'}) + \tilde{R}_{k'}(\omega; t) + W_{k'}(\omega; t),$$

for $k' \in \{k, l\}$ and $\omega = 1, \dots, n$. We define the following estimator for $\mathcal{C}_{kl}(\xi)$.

$$\mathcal{C}_{kl}^{est,n}(\xi) := \left| \widehat{\mathcal{A}_{kl}^{est,n}}(\xi) \right| / \sqrt{\left| \widehat{\mathcal{A}_{kk}^{est,n}}(\xi) \widehat{\mathcal{A}_{ll}^{est,n}}(\xi) \right|}, \quad \text{for all } \xi \in \mathbb{R},$$

[†]: Observed task-fMRI BOLD signals are $Y_k(\omega; t) = \beta_k(\omega) \times N * h_k(t - t_{0,k}) + R_k(\omega; t)$, where $R_k(\omega; t)$ are true reference signals. However, the true reference signals are not observable in applications and should be estimated by $\tilde{R}_k(\omega; t)$ using the AMUSE algorithm. The corresponding estimation bias $R_k(\omega; t) - \tilde{R}_k(\omega; t)$ is denoted by $W_k(\omega; t)$. Hence, we have $Y_k(\omega; t) = \beta_k(\omega) \times N * h_k(t - t_{0,k}) + \tilde{R}_k(\omega; t) + W_k(\omega; t)$, which is just a representation of $Y_k(\omega; t) = \beta_k(\omega) \times N * h_k(t - t_{0,k}) + R_k(\omega; t)$.

where hat (\cdot) denotes the Fourier transform and

$$\begin{aligned} \mathcal{A}_{kl}^{est,n}(s) &:= \frac{1}{T+1} \sum_{t \in \{\tau\Delta\}_{\tau=0}^T} \left[\frac{1}{n} \sum_{\omega=1}^n \{Y_k(\omega; t - U(\omega)) Y_l(\omega; t + s - U(\omega))\} \right] \\ &\quad - \frac{1}{T+1} \sum_{t \in \{\tau\Delta\}_{\tau=0}^T} \left[\frac{1}{n} \sum_{\omega=1}^n \left\{ \tilde{R}_k(\omega; t - U(\omega)) \tilde{R}_l(\omega; t + s - U(\omega)) \right\} \right]. \end{aligned}$$

Then we have the following asymptotic behavior of $C_{kl}^{est,n}(\xi)$ as $n \rightarrow \infty$.

$$\mathbb{P} \left\{ \lim_{n \rightarrow \infty} C_{kl}^{est,n}(\xi) = \frac{\left| \mathbb{E}(\beta_k \beta_l) \frac{\widehat{h}_k(\xi) \widehat{h}_l(\xi)}{|\widehat{h}_k(\xi) \widehat{h}_l(\xi)|} e^{2\pi i \xi(t_{0,k} - t_{0,l})} + \frac{\Sigma_{kl}}{(T+1) |\widehat{N}(\xi)|^2 |\widehat{h}_k(\xi) \widehat{h}_l(\xi)|} \right|}{\sqrt{\left(\mathbb{E}(\beta_k^2) + \frac{\Sigma_{kk}}{(T+1) |\widehat{N}(\xi) \widehat{h}_k(\xi)|^2} \right) \left(\mathbb{E}(\beta_l^2) + \frac{\Sigma_{ll}}{(T+1) |\widehat{N}(\xi) \widehat{h}_l(\xi)|^2} \right)}}} \right\} = 1. \quad (\text{B.2})$$

Proof. For each pair $(s, t) \in \mathcal{T}^2$, the strong law of large numbers implies that there exists $\mathcal{N}_{s,t} \in 2^\Omega$ depending on the pair (s, t) such that $\mathbb{P}(\mathcal{N}_{s,t}) = 0$ and

$$\begin{aligned} &\frac{1}{n} \sum_{\omega=1}^n \left[\{Y_k(\omega; t - U(\omega)) Y_l(\omega; t + s - U(\omega))\} - \left\{ \tilde{R}_k(\omega; t - U(\omega)) \tilde{R}_l(\omega; t + s - U(\omega)) \right\} \right] \\ &\rightarrow \mathbb{E} \{Y_k(t - U) Y_l(t + s - U)\} - \mathbb{E} \left\{ \tilde{R}_k(t - U) \tilde{R}_l(t + s - U) \right\} =: \mathcal{D}_{kl}(t, s), \end{aligned}$$

in $\Omega - \mathcal{N}_{s,t}$ as $n \rightarrow \infty$. Then we have

$$\lim_{n \rightarrow \infty} \mathcal{A}_{kl}^{est,n}(s) = \frac{1}{T+1} \sum_{t \in \{\tau\Delta\}_{\tau=0}^T} \mathcal{D}_{kl}(t, s) \quad (\text{B.3})$$

for all $s \in \mathcal{T}$ in $\Omega - \mathcal{N}$, where $\mathcal{N} := \bigcup_{s,t \in \mathcal{T}} \mathcal{N}_{s,t}$. The limit (B.3) implies the following in $\Omega - \mathcal{N}$.

$$\begin{aligned} \lim_{n \rightarrow \infty} \widehat{\mathcal{A}_{kl}^{est,n}}(\xi) &= \lim_{n \rightarrow \infty} \left\{ \frac{1}{T+1} \sum_{s \in \{\tau\Delta\}_{\tau=0}^T} \mathcal{A}_{kl}^{est,n}(s) e^{2\pi i \xi s} \right\} \\ &= \frac{1}{T+1} \sum_{s \in \{\tau\Delta\}_{\tau=0}^T} \lim_{n \rightarrow \infty} \left\{ \mathcal{A}_{kl}^{est,n}(s) \right\} e^{2\pi i \xi s} \\ &= \frac{1}{T+1} \sum_{t \in \{\tau\Delta\}_{\tau=0}^T} \left\{ \frac{1}{T+1} \sum_{s \in \{\tau\Delta\}_{\tau=0}^T} \mathcal{D}_{kl}(t, s) e^{2\pi i \xi s} \right\} \end{aligned}$$

for all $\xi \in \mathbb{R}$. In the derivation above, we change the order of summation and limit as the summation contains only finitely many terms. Since $\frac{1}{T+1} \sum_{s \in \{\tau\Delta\}_{\tau=0}^T} \mathcal{D}_{kl}(t, s) e^{2\pi i \xi s}$ is the Fourier transform of $\mathcal{D}_{kl}(t, s)$

with respect to s , repeating the calculation strategy in (B.1), we have

$$\frac{1}{T+1} \sum_{s \in \{\tau\Delta\}_{\tau=0}^T} \mathcal{D}_{kl}(t, s) e^{2\pi i \xi s} = \mathbb{E}(\beta_k \beta_l) \frac{\overline{\widehat{h}_k(\xi)} \widehat{h}_l(\xi)}{\left| \widehat{h}_k(\xi) \widehat{h}_l(\xi) \right|} e^{2\pi i \xi (t_{0,k} - t_{0,l})} + \frac{\Sigma_{kl}}{(T+1) \left| \widehat{N}(\xi) \right|^2 \left| \widehat{h}_k(\xi) \widehat{h}_l(\xi) \right|},$$

which does not depend on t . Then we have

$$\lim_{n \rightarrow \infty} \widehat{\mathcal{A}}_{kl}^{est,n}(\xi) = \mathbb{E}(\beta_k \beta_l) \frac{\overline{\widehat{h}_k(\xi)} \widehat{h}_l(\xi)}{\left| \widehat{h}_k(\xi) \widehat{h}_l(\xi) \right|} e^{2\pi i \xi (t_{0,k} - t_{0,l})} + \frac{\Sigma_{kl}}{(T+1) \left| \widehat{N}(\xi) \right|^2 \left| \widehat{h}_k(\xi) \widehat{h}_l(\xi) \right|} \quad (\text{B.4})$$

for all $\xi \in \mathbb{R}$ in $\Omega - \mathcal{N}$. The limit (B.4) implies

$$\begin{aligned} \lim_{n \rightarrow \infty} \mathcal{C}_{kl}^{est,n}(\xi) &= \left| \lim_{n \rightarrow \infty} \widehat{\mathcal{A}}_{kl}^{est,n}(\xi) \right| / \sqrt{\left| \lim_{n \rightarrow \infty} \widehat{\mathcal{A}}_{kk}^{est,n}(\xi) \times \lim_{n \rightarrow \infty} \widehat{\mathcal{A}}_{ll}^{est,n}(\xi) \right|} \\ &= \frac{\left| \mathbb{E}(\beta_k \beta_l) \frac{\overline{\widehat{h}_k(\xi)} \widehat{h}_l(\xi)}{\left| \widehat{h}_k(\xi) \widehat{h}_l(\xi) \right|} e^{2\pi i \xi (t_{0,k} - t_{0,l})} + \frac{\Sigma_{kl}}{(T+1) \left| \widehat{N}(\xi) \right|^2 \left| \widehat{h}_k(\xi) \widehat{h}_l(\xi) \right|} \right|}{\sqrt{\left(\mathbb{E}(\beta_k^2) + \frac{\Sigma_{kk}}{(T+1) \left| \widehat{N}(\xi) \widehat{h}_k(\xi) \right|^2} \right) \left(\mathbb{E}(\beta_l^2) + \frac{\Sigma_{ll}}{(T+1) \left| \widehat{N}(\xi) \widehat{h}_l(\xi) \right|^2} \right)}} \end{aligned}$$

for all $\xi \in \mathbb{R}$ in $\Omega - \mathcal{N}$. Since $\mathbb{P}(\mathcal{N}) = \mathbb{P}\left(\bigcup_{s,t \in \mathcal{T}} \mathcal{N}_{s,t}\right) \leq \sum_{s,t \in \mathcal{T}} \mathbb{P}(\mathcal{N}_{s,t}) = 0$, the desired result (B.2) follows. \square

Proof of Theorem 2 in the manuscript: In the following equation provided in Theorem 1, \mathbf{P} is a permutation matrix and $\mathbf{\Lambda}$ is a diagonal matrix.

$$\begin{pmatrix} 1 & 1 \\ \frac{1}{\beta^*} & 0 \end{pmatrix} = \mathbf{A} \mathbf{\Lambda}^{-1} \mathbf{P}^{-1}. \quad (\text{B.5})$$

Then equation (B.5) implies $\beta^* = \beta_k(\omega) = a_{1i'}/a_{2i'}$ for some $i' \in \{1, 2\}$ and $a_{2j} = 0$ when $j \neq i'$. Furthermore, the pair $(\mathbf{A}, \mathbf{S}(\omega; t))$ also satisfies the following equation, which is provided in Theorem 1 as well.

$$\mathbf{A} \begin{pmatrix} s_1(\omega; t) \\ s_2(\omega; t) \end{pmatrix} = \begin{pmatrix} 1 & 1 \\ \frac{1}{\beta^*} & 0 \end{pmatrix} \begin{pmatrix} J_k(\omega; t) \\ R_k(\omega; t - U(\omega)) \end{pmatrix} = \begin{pmatrix} Y_k(\omega; t - U(\omega)) - \beta^* C_k \\ (N * h_k)(t - t_{0,k} - U(\omega)) - C_k \end{pmatrix}, \quad (\text{B.6})$$

and equation (B.6) implies $a_{2i'}s_{i'}(\omega; t) = (N * h_k)(t - t_{0,k} - U(\omega)) - C_k$. Therefore, we have

$$a_{1i'}s_{i'}(\omega; t) = \frac{a_{1i'}}{a_{2i'}} \times a_{2i'}s_{i'}(\omega; t) = \beta_k(\omega) \times \{(N * h_k)(t - t_{0,k} - U(\omega)) - C_k\} = J_k(\omega; t).$$

C The Identifiability of Task-evoked Terms

Let $U : \Omega \rightarrow \mathcal{T}$ be a uniformly distributed random variable. Identifying the task-evoked terms $P_k(\omega; t)$ from $Y_k(\omega; t) = P_k(\omega; t) + R_k(\omega; t)$ is equivalent to identifying $P_k(\omega; t - U(\omega))$ from $Y_k(\omega; t - U(\omega))$ given the auxiliary random variable $U(\omega)$, which we can assume to be known as it is artificially generated. Our proposed BOLD signal model $Y_k(\omega; t - U(\omega)) = P_k(\omega; t - U(\omega)) + R_k(\omega; t - U(\omega))$ can be represented in the following “mixing” form.

$$Y_k(\omega; t - U(\omega)) = \begin{pmatrix} 1 & 0 \\ 0 & 1 \end{pmatrix} \begin{pmatrix} P_k(\omega; t - U(\omega)) \\ R_k(\omega; t - U(\omega)) \end{pmatrix}, \quad (\text{C.1})$$

where the identity matrix mixes the source signals $P_k(\omega; t - U(\omega))$ and $R_k(\omega; t - U(\omega))$.

In this section, we provide the identifiability of the task-evoked terms $P_k(\omega; t - U(\omega)) = \beta_k(\omega)N * h_k(t - t_{0,k} - U(\omega))$ as well as reference terms $R_k(\omega; t - U(\omega))$ in (C.1), up to deterministic coefficients, among the family of *mixing forms* defined as follows.

$$\mathcal{M} := \left\{ \begin{pmatrix} s_1(\omega; t) \\ s_2(\omega; t) \end{pmatrix} \middle| \exists \mathbf{A} \in \mathbb{R}^{2 \times 2} \text{ such that } Y_k(\omega; t - U(\omega)) = \mathbf{A} \begin{pmatrix} s_1(\omega; t) \\ s_2(\omega; t) \end{pmatrix} \right\}, \quad (\text{C.2})$$

where all matrices \mathbf{A} are deterministic 2-by-2 matrices mixing *source signals* $s_1(\omega; t)$ and $s_2(\omega; t)$. Specifically, we will show that, under some probabilistic conditions, all the stochastic signals $(s_1(\omega; t), s_2(\omega; t))$ in (C.2) are proportional to $(P_k(\omega; t - U(\omega)), R_k(\omega; t - U(\omega)))$ or $(R_k(\omega; t - U(\omega)), P_k(\omega; t - U(\omega)))$. Then the task-evoked terms $P_k(\omega; t - U(\omega))$ are identifiable in \mathcal{M} in the following sense: there exist $i' \in \{1, 2\}$ and $\lambda \neq 0$ such that $s_{i'}(\omega; t) = \lambda P_k(\omega; t - U(\omega)) = \{\lambda \beta_k(\omega)\}N * h_k(t - t_{0,k} - U(\omega))$ for all $t \in \mathcal{T}$. Since the deterministic coefficient λ is canceled out in computing $\text{corr}(\beta_k, \beta_l)$, the identifiability of $P_k(\omega; t)$ up to a deterministic coefficient implies the exact identifiability of ptFC $|\text{corr}(\beta_k, \beta_l)|$.

The following theorem implies the identifiability of $P_k(\omega; t)$ and provides a formal foundation for the discussion above.

Theorem C.1. *Let $U : \Omega \rightarrow \mathcal{T}$ be uniformly distributed. Suppose $U(\omega)$, $\beta_k(\omega)$, and $\{R_k(\omega; t) | t \in \mathcal{T}\}$ are*

independent, and $R_k(\omega; t)$ is WSMZ. Furthermore, we assume that there exists a $t^* \in \mathcal{T}$ such that

$$\frac{\mathbb{E}\{P_k(t-U)P_k(t-t^*-U)\}}{\mathbb{E}\{P_k(t-U)\}^2} \neq \frac{\mathbb{E}\{R_k(t-U)R_k(t-t^*-U)\}}{\mathbb{E}\{R_k(t-U)\}^2}.$$

If there exists a WSMZ stochastic process $(s_1(\omega; t), s_2(\omega; t))$ such that $\{s_1(\omega; t)\}_{t \in \mathcal{T}}$ and $\{s_2(\omega; t)\}_{t \in \mathcal{T}}$ are uncorrelated,

$$\frac{\mathbb{E}\{s_1(t)s_1(t-t^*)\}}{\mathbb{E}\{s_1(t)\}^2} \neq \frac{\mathbb{E}\{s_2(t)s_2(t-t^*)\}}{\mathbb{E}\{s_2(t)\}^2}, \text{ and}$$

$$Y_k(\omega; t-U(\omega)) = P_k(\omega; t-U(\omega)) + R_k(\omega; t-U(\omega)) = \mathbf{A} \begin{pmatrix} s_1(\omega; t) \\ s_2(\omega; t) \end{pmatrix}$$

for some deterministic 2-by-2 matrix \mathbf{A} , then there exists a permutation matrix \mathbf{P} and a non-singular diagonal matrix $\mathbf{\Lambda}$ such that

$$\begin{pmatrix} P_k(\omega; t-U(\omega)) \\ R_k(\omega; t-U(\omega)) \end{pmatrix} = \mathbf{P}\mathbf{\Lambda} \begin{pmatrix} s_1(\omega; t) \\ s_2(\omega; t) \end{pmatrix}. \quad (\text{C.3})$$

Remark: (i) Our discussion of identifiability presented at the beginning of this section is based on (C.3). (ii) Since $\mathbb{E}\beta_k = \mathbb{E}R_k(t) = 0$ for all t , we have $\mathbb{E}\{P_k(t_1)R_k(t_2)\} = 0$ for all $t_1, t_2 \in \mathcal{T}$, i.e., $P_k(\omega; t_1)$ and $R_k(\omega; t_2)$ are uncorrelated. (iii) One can verify that $P_k(\omega; t-U(\omega)) = \beta_k(\omega)N * h_k(t-t_{0,k}-U(\omega))$ is WSMZ. (iv) Since $R_k(\omega; t)$ is WSMZ, Lemma B.2 in the preceding section shows that $R_k(\omega; t-U(\omega))$ is WSMZ as well.

Based on these remarks, Theorem C.1 is a straightforward result following from the Theorem 2 of Tong et al. (1991).

D The Performance of ptFCE in Estimating ptFCs

In this section, we analyze the performance of the ptFCE algorithm in terms of estimation bias and variance from both theoretical and simulational perspectives.

We first provide the estimation bias mechanism of the ptFCE algorithm motivated by

$$\mathbb{P} \left\{ \lim_{n \rightarrow \infty} C_{kl}^{est,n}(\xi) = \frac{\left| \mathbb{E}(\beta_k \beta_l) \frac{\widehat{h}_k(\xi) \widehat{h}_l(\xi)}{|\widehat{h}_k(\xi) \widehat{h}_l(\xi)|} e^{2\pi i \xi(t_{0,k} - t_{0,l})} + \frac{\Sigma_{kl}}{(T+1)|\widehat{N}(\xi)|^2 |\widehat{h}_k(\xi) \widehat{h}_l(\xi)|} \right|}{\sqrt{\left(\mathbb{E}(\beta_k^2) + \frac{\Sigma_{kk}}{(T+1)|\widehat{N}(\xi) \widehat{h}_k(\xi)|^2} \right) \left(\mathbb{E}(\beta_l^2) + \frac{\Sigma_{ll}}{(T+1)|\widehat{N}(\xi) \widehat{h}_l(\xi)|^2} \right)}}} \right\} = 1, \quad (\text{D.1})$$

which is from Web Theorem B.2. Because the quantities in

$$\Sigma_{kk} / [(T+1)|\widehat{N}(\xi) \widehat{h}_k(\xi)|^2] \approx 0, \quad \Sigma_{ll} / [(T+1)|\widehat{N}(\xi) \widehat{h}_l(\xi)|^2] \approx 0.$$

are not exactly zeros, the asymptotic estimation bias

$$\left| \lim_{n \rightarrow \infty} C_{kl}^{est,n}(\xi) - C_{kl}(\xi) \right| = \left| \lim_{n \rightarrow \infty} C_{kl}^{est,n}(\xi) - \frac{|\mathbb{E}(\beta_k \beta_l)|}{\sqrt{\mathbb{E}(\beta_k^2) \mathbb{E}(\beta_l^2)}} \right|$$

always exists. We further model that approximation residual $W_{k'}(\omega; t) = R_{k'}(\omega; t) - \widetilde{R}_{k'}(\omega; t)$ at different nodes are independent, implying $\Sigma_{kl} = 0$ in (D.1). Then the following inequality, as a result of (D.1), indicates that our ptFCE algorithm tends to underestimate ptFC.

$$\begin{aligned} \lim_{n \rightarrow \infty} C_{kl}^{est,n}(\xi) &=_{a.s.} \frac{|\mathbb{E}(\beta_k \beta_l)|}{\sqrt{\left(\mathbb{E}(\beta_k^2) + \frac{\Sigma_{kk}}{(T+1)|\widehat{N}(\xi) \widehat{h}_k(\xi)|^2} \right) \left(\mathbb{E}(\beta_l^2) + \frac{\Sigma_{ll}}{(T+1)|\widehat{N}(\xi) \widehat{h}_l(\xi)|^2} \right)}} \\ &\leq \frac{|\mathbb{E}(\beta_k \beta_l)|}{\sqrt{\mathbb{E}(\beta_k^2) \mathbb{E}(\beta_l^2)}} = |\text{corr}(\beta_k, \beta_l)|. \end{aligned} \quad (\text{D.2})$$

Furthermore, the larger the variance of the noise $\epsilon_k(\omega; t)$ in

$$Y_k(\omega; t) = \beta_k(\omega) \times (N * h_k)(t - t_{0,k}) + R_k(\omega; t), \quad t \in \mathcal{T}, \quad k = 1, \dots, K, \quad \omega \in \Omega,$$

the less accurate is the approximation $R_{k'}(\omega; t) \approx \widetilde{R}_{k'}(\omega; t)$ and the larger Σ_{kk} and Σ_{ll} in the inequality (D.2). Hence, the larger the variance of noise $\epsilon_k(\omega; t)$, the larger the underestimation bias. The formula above also indicates that the larger the underlying ptFC, the larger the underestimation bias. Subsequent simulations confirm all the conclusions on bias presented herein. We also show that the underestimation bias is moderate in general in terms of estimating ptFCs.

We present the performance of ptFCE in estimating ptFC by investigating estimation bias and vari-

Table 3: The summaries of the estimated $\hat{\rho}$ in different underlying ptFC ρ scenarios. The percentage in the parenthesis after each mean shows the corresponding relative bias $(\hat{\rho} - \rho)/\rho$, where the minus signs indicate underestimation.

	$\rho = 0.25$		$\rho = 0.5$		$\rho = 0.75$	
	mean	sd	mean	sd	mean	sd
$n = 50$	0.255 (2%)	0.120	0.456 (-8.8%)	0.114	0.670 (-10.7%)	0.081
$n = 100$	0.246 (-1.6%)	0.093	0.460 (-8%)	0.079	0.671 (-10.5%)	0.055
$n = 308$	0.248 (-0.8%)	0.055	0.457 (-8.6%)	0.047	0.670 (-10.7%)	0.030
$n = 1000$	0.246 (-1.6%)	0.028	0.462 (-7.6%)	0.026	0.675 (-10%)	0.018

ance using simulated data. Specifically, suppose the true ptFC in our simulation mechanism is ρ , and the estimated ptFC from this algorithm is $\hat{\rho}$, then we investigate bias $\hat{\rho} - \rho$ and the variance of $\hat{\rho}$. We implement the following data-generating mechanism, compatible with the definition of ptFC. The main steps of this mechanism are the following, while the details are provided in Appendix E.

Mechanism 0: Step 1, we generate random coefficients $(\beta_1(\omega), \beta_2(\omega))^T \sim N_2(\mathbf{0}, (\sigma_{ij})_{1 \leq i, j \leq 2})$ for $\omega = 1, \dots, n$, and $\rho := |\sigma_{12}/\sqrt{\sigma_{11}\sigma_{22}}|$ is the true underlying ptFC between synthetic nodes 1 and 2. **Step 2**, we generate reference signals $\{R_{k'}(\omega; \tau\Delta) = Q_{k'}(\omega; \tau\Delta) + \epsilon_{k'}(\omega; \tau\Delta)\}_{\tau=0}^T$ for $\omega = 1, \dots, n$ and $k' \in \{1, 2\}$, where the $2nT$ noise values $\{\epsilon_{k'}(\omega; \tau\Delta) | k' = 1, 2; \omega = 1, \dots, n; \tau = 0, \dots, T\} \sim_{iid} N(0, V)$. **Step 3**, we compute the signals $\{Y_{k'}(\omega; \tau\Delta) | k' = 1, 2\}_{\tau=0}^T$, for $\omega = 1, \dots, n$, by $Y_{k'}(\omega; \tau\Delta) = 9000 + \beta_{k'}(\omega) \times (N * h_{k'}) (\tau\Delta) + R_{k'}(\omega; \tau\Delta)$.

We investigate sample sizes $n \in \{50, 100, 308, 1000\}$, where 308 is the sample size of the HCP dataset used to obtain the results in our paper. We apply the ptFCE algorithm to estimate the underlying ρ from synthetic signals. The corresponding estimate is denoted by $\hat{\rho}$. For each $\rho \in \{0.25, 0.5, 0.75\}$, we repeat this procedure 500 times. The resulting estimates $\hat{\rho}$ are summarized in Web Table 3 and Web Figure 4.

Additionally, we investigate the influence of random noise $\{\epsilon_{k'}(\omega; \tau\Delta)\}_{k', \tau, \omega} \sim_{iid} N(0, V)$ on the ptFCE algorithm. Specifically, we fix sample size $n = 308$; for each $\lambda \in [0.5, 5]$, we conduct the 500-run simulation study described above except we change the random noise to $\{\epsilon_{k'}(\omega; \tau\Delta)\}_{k', \tau, \omega} \sim_{iid} N(0, \lambda V)$. For each λ and simulation run r , the estimated ptFC between synthetic nodes is denoted as $\hat{\rho}_\lambda^{(r)}$, then we obtain 500 curves $\{\hat{\rho}_\lambda^{(r)} | \lambda \in [0.5, 5]\}_{r=1}^{500}$ presented in Web Figure 5.

As expected from the theoretical analysis of the bias mechanism, our proposed ptFCE algorithm tends to underestimate true ptFCs, see Web Table 3 and Web Figures 4 and 5. But Web Table 3 shows that the bias is moderate. Simulations also confirm other conclusions on estimation bias presented in the theoretical analysis above. Additionally, Web Figure 3 shows that the magnitude of noise $\epsilon_k(\omega; t)$ does not influence the variance of the ptFCE estimates. The increase in sample size reduces estimation

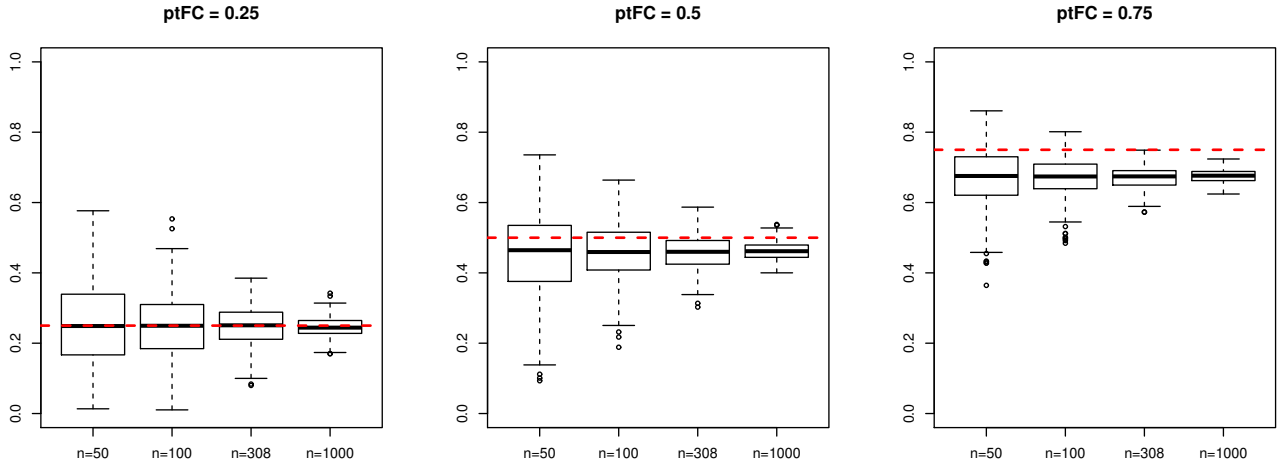


Figure 4: The boxplots summarizing the estimated $\hat{\rho}$ in different underlying ptFC ρ and different sample sizes n scenarios.

variance.

E Data-generating Mechanisms for Simulations

In this section, we provide the details of Mechanisms 0, 1, and 2 for generating synthetic signals in simulation studies in our paper. To mimic the HCP data of interest, we apply the following parameters in the two data-generating mechanisms.

- Repeation time $\Delta = 0.72$ (seconds)
- Number of observation time points $T = 283$.
- The task of interest (squeezing right toes) is presented by the stimulus signal $N(t) = \mathbf{1}_{[86.5,98.5)}(t) + \mathbf{1}_{[162,174)}(t)$.
- The tasks that are not of interest are presented by stimulus signals $\tilde{N}_1(t) = \mathbf{1}_{[71.35,83.35)}(t) + \mathbf{1}_{[177.125,189.125)}(t)$, $\tilde{N}_2(t) = \mathbf{1}_{[11,23)}(t) + \mathbf{1}_{[116.63,128.63)}(t)$, $\tilde{N}_3(t) = \mathbf{1}_{[26.13,38.13)}(t) + \mathbf{1}_{[146.88,158.88)}(t)$, and $\tilde{N}_4(t) = \mathbf{1}_{[56.26,68.26)}(t) + \mathbf{1}_{[131.75,143.75)}(t)$. They correspond to the tasks of squeezing left toes, squeezing left/right fingers, and moving tongue.
- HRF functions h_k and $\tilde{h}_{k,\gamma}$, for $k \in \{1, 3\}$ and $\gamma \in \{1, 2, 3, 4\}$, are the double-gamma variate functions implemented in the R function `canonicalHRF` with parameters `a1= 4`, `a2= 10`, `b1= 0.8`,

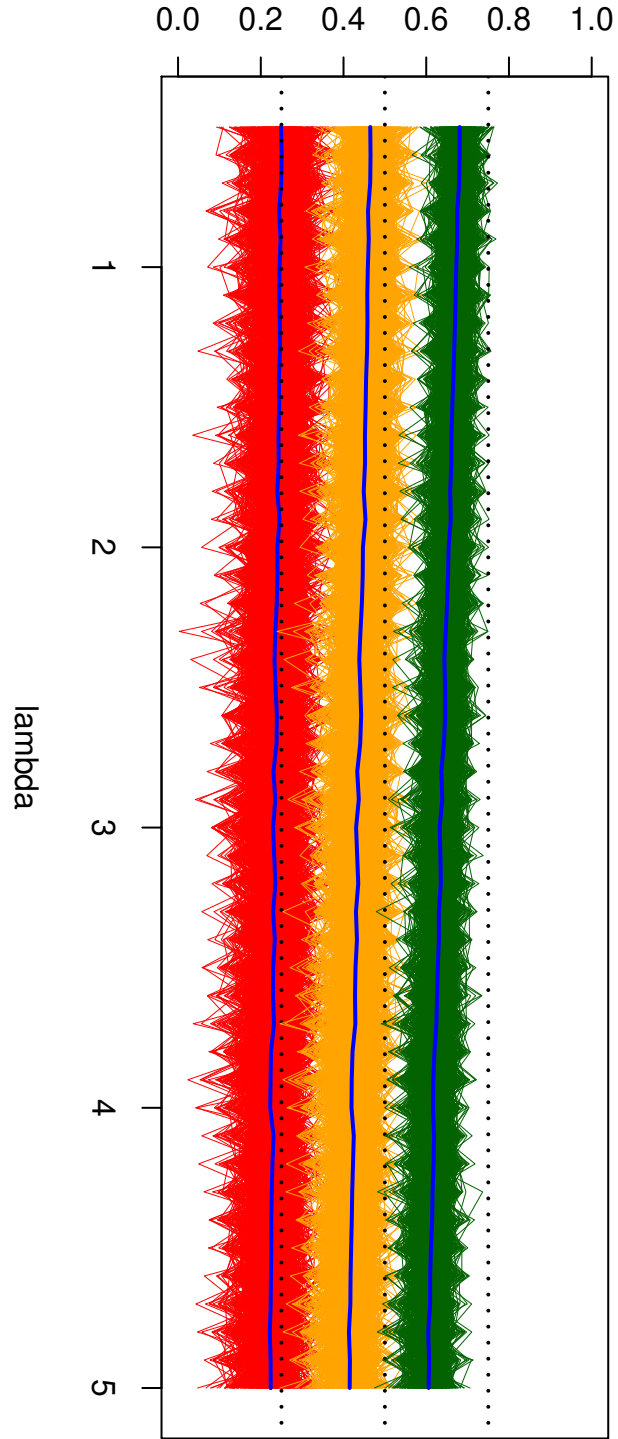


Figure 5: The red, orange, and green curves present the collections $\{\hat{\rho}_\lambda^{(r)} | \lambda \in [0.5, 5]\}_{r=1}^{500}$ corresponding to underlying ptFC $\rho = 0.25, 0.5, 0.75$. The three blue solid curves present the mean curves $\{\frac{1}{500} \sum_{r=1}^{500} \hat{\rho}_\lambda^{(r)} | \lambda \in [0.5, 5]\}$ in the three underlying ptFC scenarios, and the three black dotted lines present the three underlying ptFC.

$b_2= 0.8$, $c= 0.4$; HRF functions h_2 and $\tilde{h}_{2,\gamma}$, for $\gamma \in \{1,2,3,4\}$, are the same function with parameters $a_1= 8$, $a_2= 14$, $b_1= 1$, $b_2= 1$, $c= 0.3$. It is important to emphasize that none of the HRFs herein is canonical. The curves of all HRF functions used in our simulations studies are presented in Web Figure 6.

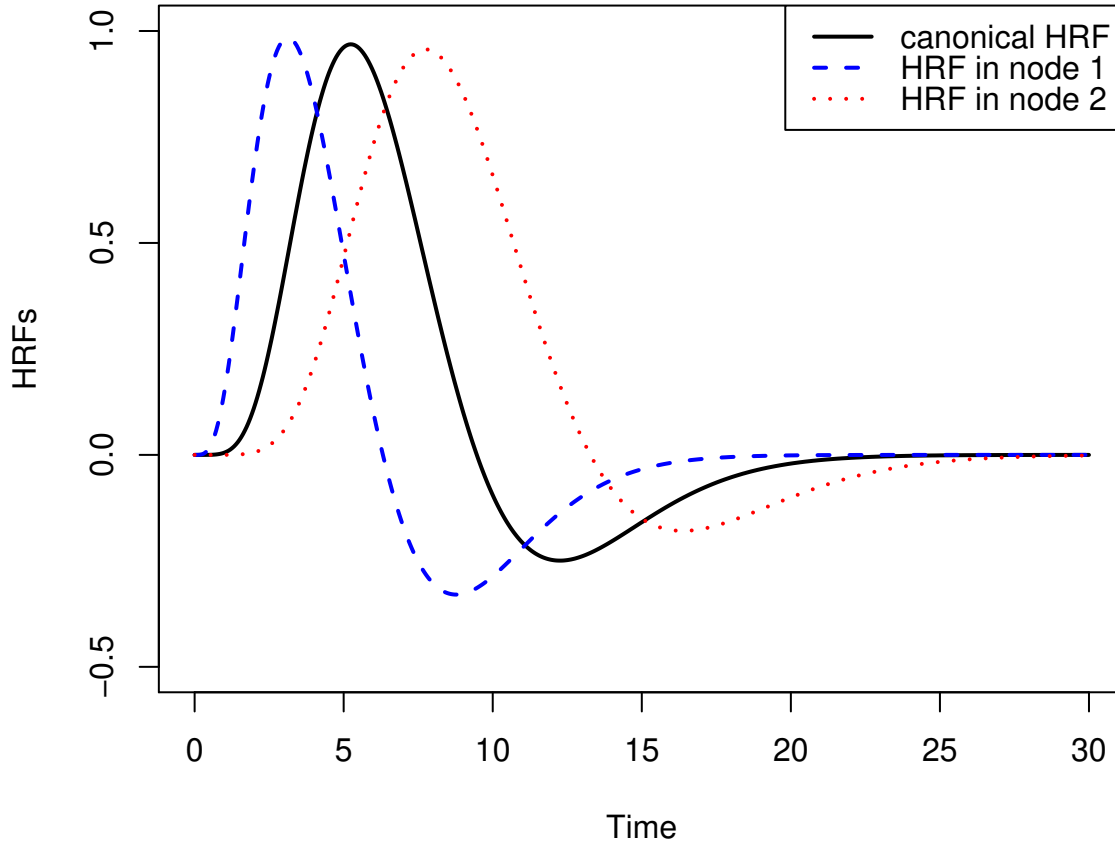


Figure 6: The black solid curve presents the canonical HRF (the R function `canonicalHRF` with default parameters). The blue dashed curve presents the R function `canonicalHRF` with parameters $a_1= 4$, $a_2= 10$, $b_1= 0.8$, $b_2= 0.8$, $c= 0.4$. The red dotted curve presents the R function `canonicalHRF` with parameters $a_1= 8$, $a_2= 14$, $b_1= 1$, $b_2= 1$, $c= 0.3$.

E.1 Mechanism 0

This mechanism is based on the task-fMRI BOLD signal model proposed in our paper. Specifically, we implement the following model to generate synthetic data.

$$Y_{k'}(\omega; t) = 9000 + \beta_{k'} \times N * h_{k'}(t) + \left\{ \sum_{\gamma=1}^4 \beta_{k',\gamma}(\omega) \times \tilde{N}_\gamma * \tilde{h}_{k',\gamma}(t) \right\} + \epsilon_{k'}(\omega; t), \quad (\text{E.1})$$

where $t \in \mathcal{T} = \{\tau\Delta\}_{\tau=0}^T$ and $k' \in \{1, 2\}$.

We generate signals $\{(Y_1(\omega; \tau\Delta), Y_2(\omega; \tau\Delta))_{\tau=0}^T\}$, for $\omega = 1, \dots, n$, by the following steps.

- **Step 1:** Generate bivariate normal random vectors $(\beta_1(\omega), \beta_2(\omega))^T \sim_{i.i.d.} N_2((0, 0)^T, (\sigma_{ij})_{1 \leq i, j \leq 2})$ for $\omega = 1, \dots, n$, where $\rho := |\sigma_{12}/\sqrt{\sigma_{11}\sigma_{22}}|$ is the true underlying ptFC, and

$$\sigma_{11} = 2, \quad \sigma_{22} = 3, \quad \sigma_{12} = \rho \times \sqrt{\sigma_{11}\sigma_{22}}. \quad (\text{E.2})$$

- **Step 2:** For each $\gamma \in \{1, 2, 3, 4\}$, generate bivariate normal random vector

$$\begin{pmatrix} \beta_{1,\gamma}(\omega) \\ \beta_{2,\gamma}(\omega) \end{pmatrix} \sim_{i.i.d.} N_2 \left(\begin{pmatrix} 0 \\ 0 \end{pmatrix}, \begin{pmatrix} 2 & 0.3 \times \sqrt{2 \times 3} \\ 0.3 \times \sqrt{2 \times 3} & 3 \end{pmatrix} \right),$$

for $\omega = 1, \dots, n$. The four collections $\{(\beta_{1,\gamma}(\omega), \beta_{2,\gamma}(\omega))^T\}_{\omega=1}^n$, for $\gamma \in \{1, 2, 3, 4\}$, are independently generated.

- **Step 3:** For each fixed $\omega \in \{1, \dots, n\}$, generate (white) noise as follows.

$$\begin{pmatrix} \epsilon_1(\omega; \tau\Delta) \\ \epsilon_2(\omega; \tau\Delta) \end{pmatrix} \sim_{i.i.d.} N_2 \left(\begin{pmatrix} 0 \\ 0 \end{pmatrix}, \begin{pmatrix} 30 & 0 \\ 0 & 30 \end{pmatrix} \right), \quad \text{for } \tau = 0, \dots, T.$$

The n collections $\{(\epsilon_1(\omega; \tau\Delta), \epsilon_2(\omega; \tau\Delta))_{\tau=0}^T\}$, for $\omega \in \{1, \dots, n\}$, are independently generated.

- **Step 4:** Compute the signals $\{(Y_1(\omega; \tau\Delta), Y_2(\omega; \tau\Delta))_{\tau=0}^T\}$, for $\omega = 1, \dots, n$, by model (E.1).

A pair of simulated $\{(Y_1(\omega; \tau\Delta), Y_2(\omega; \tau\Delta))_{\tau=0}^T\}$ using Mechanisms 0 is presented in Web Figure 7.

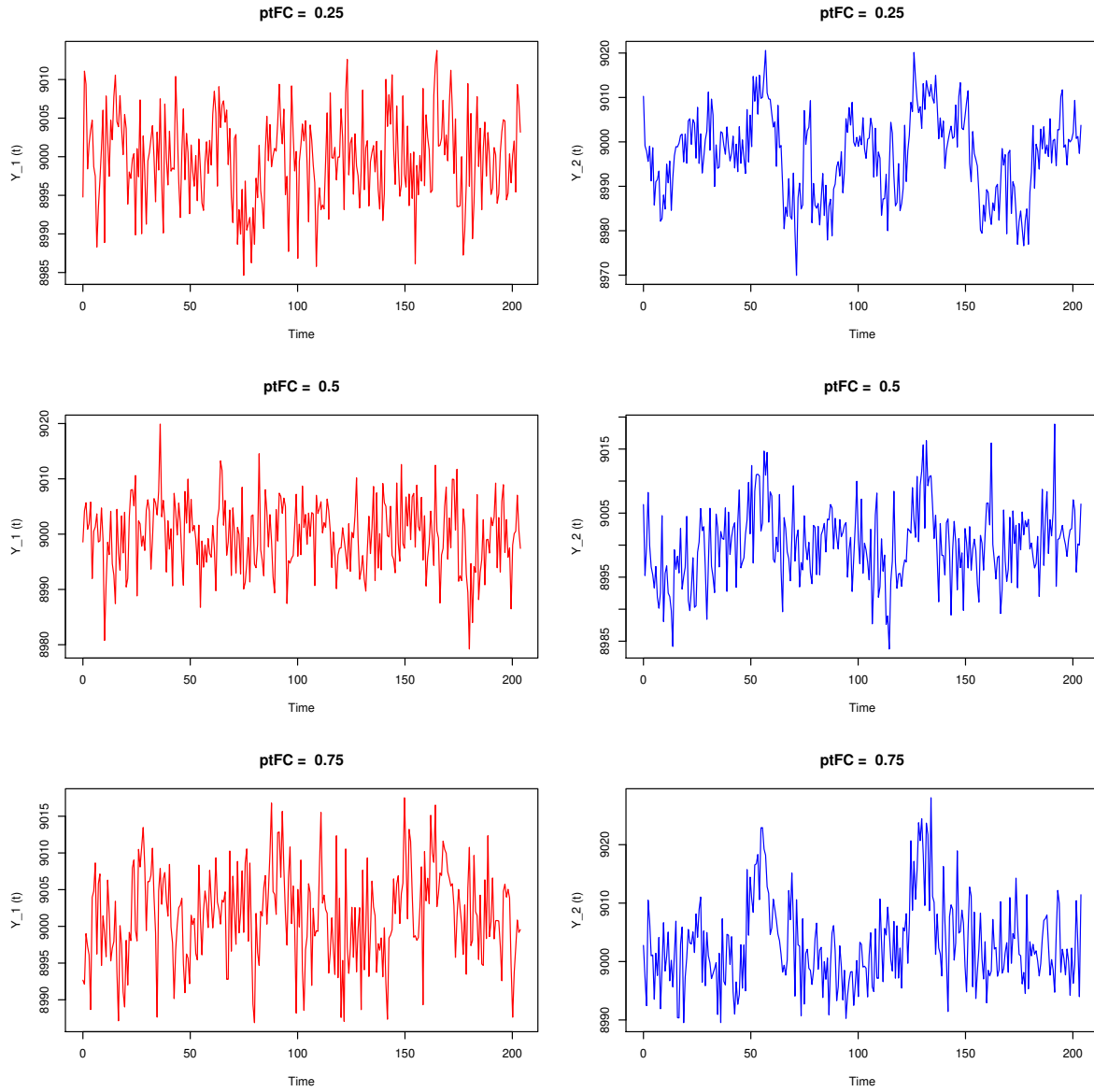


Figure 7: Left panels present signals generated for node 1, and right panels present signals generated for node 2. The underlying $ptFC$ s for pairs in the upper, middle, and lower rows are 0.25, 0.5, and 0.75, respectively.

E.2 Mechanism 1

Mechanism 1 is very similar to Mechanism 0 and is based on (E.1) as well, except for $k' \in \{1, 2, 3\}$. We generate signals $\{(Y_1(\omega; \tau\Delta), Y_2(\omega; \tau\Delta), Y_3(\omega; \tau\Delta))\}_{\tau=0}^T$, for $\omega = 1, \dots, n$, using the following steps.

- **Step 1:** Generate normal random vectors $(\beta_1(\omega), \beta_2(\omega), \beta_3(\omega))^T \sim_{i.i.d.} N_3(\mathbf{0}, (\sigma_{ij})_{1 \leq i, j \leq 3})$ for $\omega = 1, \dots, n$, where

$$(\sigma_{ij})_{1 \leq i, j \leq 3} = \begin{pmatrix} 2 & \rho_{12} \times \sqrt{2 \times 3} & 0 \\ \rho_{12} \times \sqrt{2 \times 3} & 3 & \rho_{23} \times \sqrt{2 \times 3} \\ 0 & \rho_{23} \times \sqrt{2 \times 3} & 2 \end{pmatrix}, \quad (\text{E.3})$$

and $\rho_{ij} := |\sigma_{ij} / \sqrt{\sigma_{ii}\sigma_{jj}}|$ for $(i, j) \in \{(1, 2), (2, 3)\}$ are the true underlying ptFCs.

- **Step 2:** For each $\gamma \in \{1, 2, 3, 4\}$, generate bivariate normal random vector

$$\begin{pmatrix} \beta_{1,\gamma}(\omega) \\ \beta_{2,\gamma}(\omega) \\ \beta_{3,\gamma}(\omega) \end{pmatrix} \sim_{i.i.d.} N_3 \left(\begin{pmatrix} 0 \\ 0 \\ 0 \end{pmatrix}, \begin{pmatrix} 2 & 0.3 \times \sqrt{2 \times 3} & 0 \\ 0.3 \times \sqrt{2 \times 3} & 3 & 0.3 \times \sqrt{2 \times 3} \\ 0 & 0.3 \times \sqrt{2 \times 3} & 2 \end{pmatrix} \right),$$

for $\omega = 1, \dots, n$. The four collections $\{(\beta_{1,\gamma}(\omega), \beta_{2,\gamma}(\omega), \beta_{3,\gamma}(\omega))\}_{\omega=1}^n$, for $\gamma \in \{1, 2, 3, 4\}$, are independently generated.

- **Step 3:** For each fixed $\omega \in \{1, \dots, n\}$, generate (white) noise as follows.

$$\begin{pmatrix} \epsilon_1(\omega; \tau\Delta) \\ \epsilon_2(\omega; \tau\Delta) \\ \epsilon_3(\omega; \tau\Delta) \end{pmatrix} \sim_{i.i.d.} N_3 \left(\begin{pmatrix} 0 \\ 0 \\ 0 \end{pmatrix}, \begin{pmatrix} 30 & 0 & 0 \\ 0 & 30 & 0 \\ 0 & 0 & 30 \end{pmatrix} \right), \text{ for } \tau = 0, \dots, T.$$

The n collections $\{(\epsilon_1(\omega; \tau\Delta), \epsilon_2(\omega; \tau\Delta), \epsilon_3(\omega; \tau\Delta))\}_{\tau=0}^T$, for $\omega \in \{1, \dots, n\}$, are independently generated.

- **Step 4:** Compute the signals $\{(Y_1(\omega; \tau\Delta), Y_2(\omega; \tau\Delta), Y_3(\omega; \tau\Delta))\}_{\tau=0}^T$, for $\omega = 1, \dots, n$, by model (E.1).

E.3 Mechanism 2

This mechanism is motivated by the Pearson correlation approach and implemented by the following steps.

- **Step 1:** For each fixed $\omega \in \{1, \dots, n\}$, we independently generate $(\epsilon_1(\omega; \tau\Delta), \epsilon_2(\omega; \tau\Delta), \epsilon_3(\omega; \tau\Delta))^T$, for $\tau \in \{1, \dots, T\}$, using the following distributions:

(i) If $N(\tau\Delta) = 1$, we apply

$$\begin{pmatrix} \epsilon_1(\omega; \tau\Delta) \\ \epsilon_2(\omega; \tau\Delta) \\ \epsilon_3(\omega; \tau\Delta) \end{pmatrix} \sim N_3 \left(\begin{pmatrix} 0 \\ 0 \\ 0 \end{pmatrix}, \begin{pmatrix} 30 & \varrho \times 30 & 0 \\ \varrho \times 30 & 30 & \varrho \times 30 \\ 0 & \varrho \times 30 & 30 \end{pmatrix} \right); \quad (\text{E.4})$$

if $N(\tau\Delta) = 0$, we implement

$$\begin{pmatrix} \epsilon_1(\omega; \tau\Delta) \\ \epsilon_2(\omega; \tau\Delta) \\ \epsilon_3(\omega; \tau\Delta) \end{pmatrix} \sim N_3 \left(\begin{pmatrix} 0 \\ 0 \\ 0 \end{pmatrix}, \begin{pmatrix} 30 & 0 & 0 \\ 0 & 30 & 0 \\ 0 & 0 & 30 \end{pmatrix} \right).$$

The n collections $\{(\epsilon_1(\omega; \tau\Delta), \epsilon_2(\omega; \tau\Delta), \epsilon_3(\omega; \tau\Delta))\}_{\tau=0}^T$, for $\omega \in \{1, \dots, n\}$, are independently generated.

- **Step 2:** Compute the signals $\{(Y_1(\omega; \tau\Delta), Y_2(\omega; \tau\Delta), Y_3(\omega; \tau\Delta))\}_{\tau=0}^T$, for $\omega = 1, \dots, n$, by the following.

$$Y_{k'}(\omega; t) = 9000 + N * h_{k'}(t) + \left\{ \sum_{\gamma=1}^4 \tilde{N}_\gamma * \tilde{h}_{k', \gamma}(t) \right\} + \epsilon_{k'}(\omega; t), \quad (\text{E.5})$$

where $t \in \mathcal{T} = \{\tau\Delta\}_{\tau=0}^T$ and $k' \in \{1, 2, 3\}$.

Simulated $\{(Y_1(\omega; \tau\Delta), Y_2(\omega; \tau\Delta), Y_3(\omega; \tau\Delta))\}_{\tau=0}^T$ using Mechanisms 1 and 2, are presented in Web Figure 8.

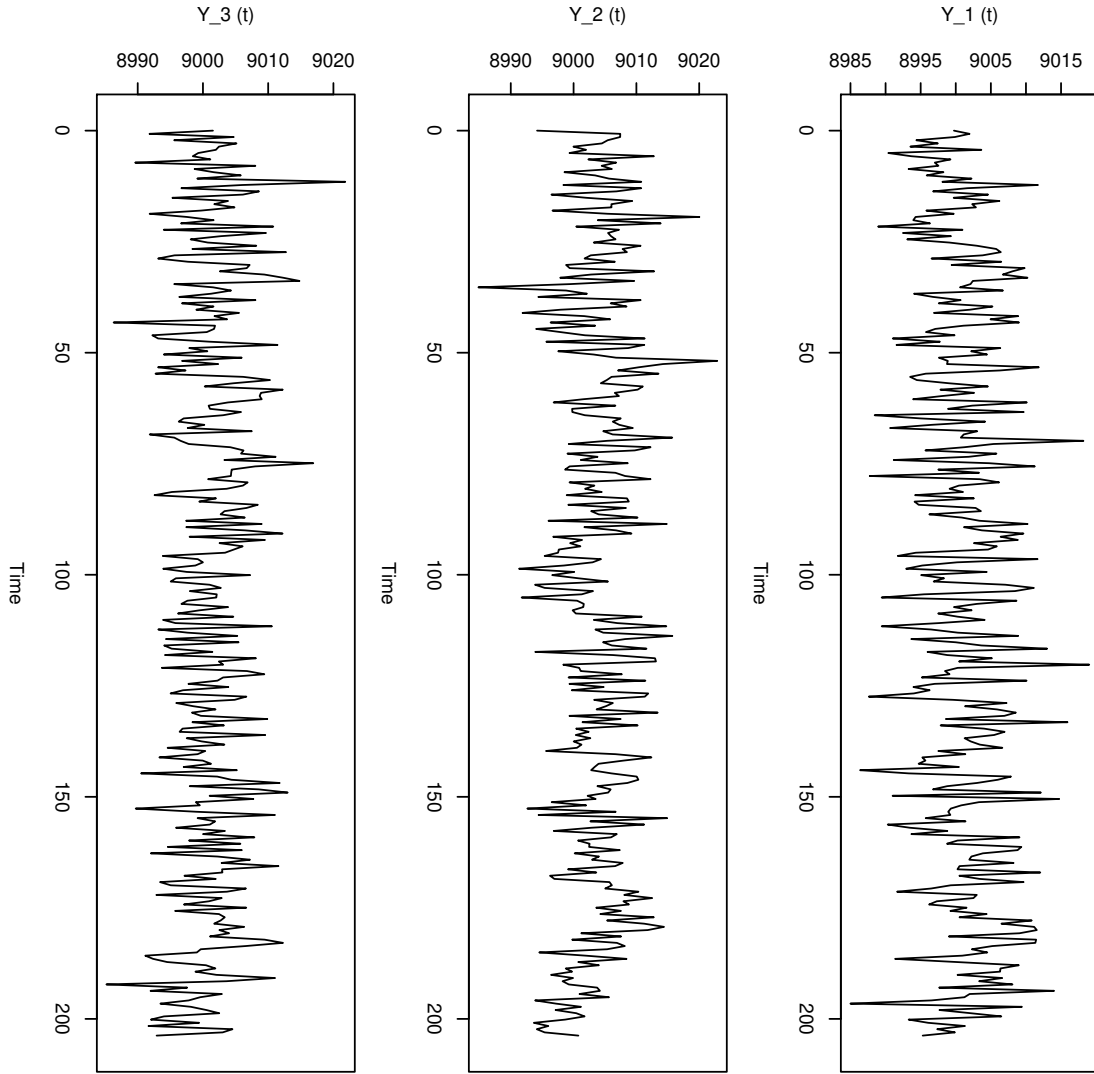


Figure 8: Signals generated for nodes 1, 2, and 3 using Mechanism 2.

F Limitations of the Pearson correlation approach

Web Figure 9 illustrates the limitations of the Pearson correlation approach defined as follows in terms of the influence of latency/HRF variance and noise.

$$|corr(P_k, P_l)| = \left| \frac{\int_{\mathcal{T}} \phi_k(t) \times \phi_l(t) \mu(dt)}{\sqrt{\int_{\mathcal{T}} |\phi_k(t)|^2 \mu(dt) \times \int_{\mathcal{T}} |\phi_l(t)|^2 \mu(dt)}} \right|. \quad (\text{F.1})$$

G Details of Beta-series Regression and Coherence Analysis

Beta-series regression: We apply the procedure described in Chapter 9.2 of [Ashby \(2019\)](#) to estimate task-evoked FC using beta-series regression, except we ignore the “nuisance term” therein. For each sub-

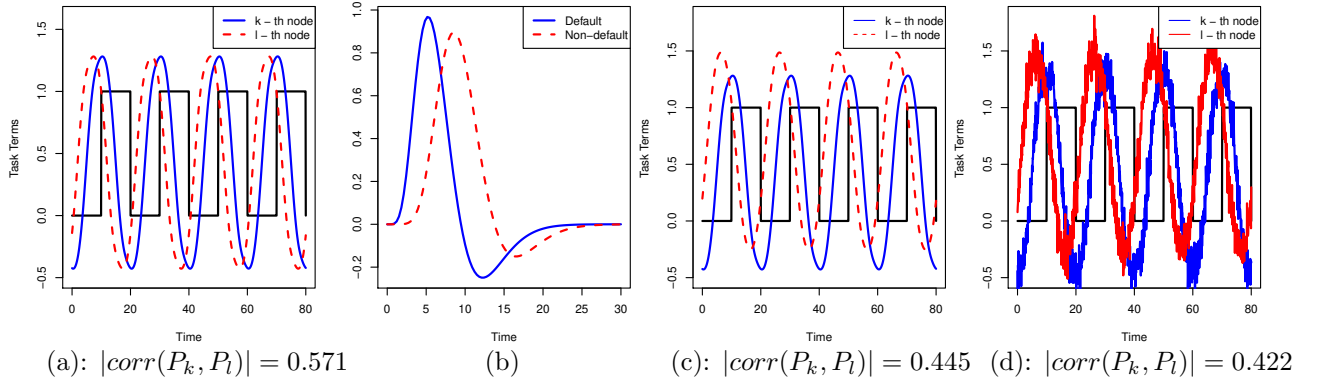


Figure 9: An example illustrating the limitations of the Pearson correlation approach in (F.1). Let $N(t) = \sum_{m=1}^4 \mathbf{1}_{(20m-10, 20m)}(t)$ be the stimulus signal of a block design, $\mathcal{T} = [0, 80]$, and h_k be the `canonicalHRF` function with default parameters in the R package `neuRosim`. h_k is illustrated by the solid blue curve in (b). Panel (a) shows the influence of the variation in latency on (F.1), where $h_l(t) = h_k(t+3)$, i.e., $t_{0,k} = -3$; the task-evoked terms at the k^{th} and l^{th} nodes are presented by blue and red curves, respectively. In (b), h_l is replaced by the `canonicalHRF` function with parameters $\mathbf{a1} = 10, \mathbf{a2} = 15, \mathbf{b1} = \mathbf{b2} = 0.9, \mathbf{c} = 0.35$, and presented by the dashed red curve. Panel (c) shows the influence of variation in HRF on (F.1), and the task-evoked terms at the k^{th} and l^{th} nodes are presented by blue and red curves, respectively, where h_l is defined in (b) as the red curve. Panel (d) is a noise-contaminated version of (c), i.e., curves of $P_k(t) + \epsilon_k(t)$ (blue) and $P_l(t) + \epsilon_l(t)$ (red) with $\epsilon_k(t), \epsilon_l(t) \sim_{iid} N(0, 0.1)$ for each t . Panel (d) shows that random noise can further influence (F.1). In panels (a,c,d), the presented $|corr(P_k, P_l)|$ is computed by (F.1).

ject ω and underlying ρ_{ij} or ϱ_{ij} with $i < j$, we apply beta-series regression to signals $\{Y_i(\omega; \tau\Delta), Y_j(\omega; \tau\Delta)\}_{\tau=0}^T$, estimate the FC evoked by the task of interest $N(t)$, and denote the estimated quantity by $\hat{\rho}_{ij,\omega}^{betaS}$. Then we compute the mean and median of $\{\hat{\rho}_{ij,\omega}^{betaS}\}_{\omega=1}^n$ across all $\omega = 1, \dots, n$ and denote them by $\hat{\rho}_{ij,\omega}^{betaS, mean}$ and $\hat{\rho}_{ij,\omega}^{betaS, median}$.

Coherence analysis: For each ω and ρ_{ij} or ϱ_{ij} , compute the coherence between signals $\{Y_i(\omega; \tau\Delta)\}_{\tau}$ and $\{Y_j(\omega; \tau\Delta)\}_{\tau}$ by the R function `coh` in package `seewave`. The coherence is a function $coh_{ij,\omega}(\xi)$ of ξ . Since HRFs act as band-pass filters (0–0.15 Hz, Aguirre et al. (1997)), compute the median of $coh_{ij,\omega}(\xi)$ across all $\xi \in (0, 0.15)$ and denote it by $\hat{\rho}_{ij,\omega}^{Coh}$. The mean and median of $\{\hat{\rho}_{ij,\omega}^{Coh}\}_{\omega=1}^n$ across all ω are denoted by $\hat{\rho}_{ij,\omega}^{Coh, mean}$ and $\hat{\rho}_{ij,\omega}^{Coh, median}$, respectively.

H Future Research

An interesting extension of our proposed model is the inclusion of an interaction term between the $P_k(\omega; t)$ and $Q_k(\omega; t)$ in model $Y_k(\omega; t) = P_k(\omega; t) + Q_k(\omega; t) + \epsilon_k(\omega; t)$. In order to experimentally validate whether the inclusion of such an interaction term would be biologically relevant, novel experimental designs would be needed. Particularly, we may consider an experiment where the subjects are at rest for a certain

period during the scanning session followed by the performance of the task. Using this design, we may obtain estimates of P_k and Q_k considering the model with and without an interaction term and discuss the biological relevance of the results. Future work may investigate this issue and develop theoretical conditions for the identifiability of terms in a model with an interaction term and estimation algorithms.

In many applications, task-evoked FC at the subject level instead of the population level is of interest. In our subsequent research, we will propose a framework parallel to the ptFC one at the subject level. Additionally, implementing the *persistent homology* (PH) framework to FC estimates is an effective way of circumventing the choice of threshold for FC measurements, e.g., see [Lee et al. \(2001\)](#). Applying the PH approach to our proposed ptFCs is left for future research as well.

References

- G. K. Aguirre, E. Zarahn, and M. D’Esposito. Empirical analyses of bold fmri statistics. *NeuroImage*, 5(3):179–197, 1997.
- F. G. Ashby. *Statistical analysis of fMRI data*. MIT press, 2019.
- D. M. Barch, G. C. Burgess, M. P. Harms, S. E. Petersen, B. L. Schlaggar, M. Corbetta, M. F. Glasser, S. Curtiss, S. Dixit, C. Feldt, et al. Function in the human connectome: task-fmri and individual differences in behavior. *Neuroimage*, 80:169–189, 2013.
- R. L. Buckner, F. M. Krienen, A. Castellanos, J. C. Diaz, and B. T. Yeo. The organization of the human cerebellum estimated by intrinsic functional connectivity. *Journal of neurophysiology*, 106(5):2322–2345, 2011.
- J. M. Cisler, K. Bush, and J. S. Steele. A comparison of statistical methods for detecting context-modulated functional connectivity in fmri. *Neuroimage*, 84:1042–1052, 2014.
- J. Cohen. A coefficient of agreement for nominal scales. *Educational and psychological measurement*, 20(1):37–46, 1960.
- J. B. Conway. *Functions of One Complex Variable I*. Springer Verlag, 1973.
- I. Cribben and M. Fiecas. Functional connectivity analyses for fmri data. *Handbook of neuroimaging data analysis*, 369, 2016.

- K. Friston, C. Frith, P. Liddle, and R. Frackowiak. Functional connectivity: the principal-component analysis of large (pet) data sets. *Journal of Cerebral Blood Flow & Metabolism*, 13(1):5–14, 1993.
- K. J. Friston, P. Jezzard, and R. Turner. Analysis of functional mri time-series. *Human brain mapping*, 1(2):153–171, 1994.
- R. M. Hutchison, T. Womelsdorf, E. A. Allen, P. A. Bandettini, V. D. Calhoun, M. Corbetta, S. Della Penna, J. H. Duyn, G. H. Glover, J. Gonzalez-Castillo, et al. Dynamic functional connectivity: promise, issues, and interpretations. *Neuroimage*, 80:360–378, 2013.
- S. E. Joel, B. S. Caffo, P. C. van Zijl, and J. J. Pekar. On the relationship between seed-based and ica-based measures of functional connectivity. *Magnetic Resonance in Medicine*, 66(3):644–657, 2011.
- S.-P. Lee, T. Q. Duong, G. Yang, C. Iadecola, and S.-G. Kim. Relative changes of cerebral arterial and venous blood volumes during increased cerebral blood flow: implications for bold fmri. *Magnetic Resonance in Medicine: An Official Journal of the International Society for Magnetic Resonance in Medicine*, 45(5):791–800, 2001.
- M. A. Lindquist et al. The statistical analysis of fmri data. *Statistical science*, 23(4):439–464, 2008.
- M. J. Lowe, M. Dzemidzic, J. T. Lurito, V. P. Mathews, and M. D. Phillips. Correlations in low-frequency bold fluctuations reflect cortico-cortical connections. *Neuroimage*, 12(5):582–587, 2000.
- L. K. Lynch, K.-H. Lu, H. Wen, Y. Zhang, A. J. Saykin, and Z. Liu. Task-evoked functional connectivity does not explain functional connectivity differences between rest and task conditions. *Human brain mapping*, 39(12):4939–4948, 2018.
- A. F. Mejia, M. B. Nebel, A. D. Barber, A. S. Choe, J. J. Pekar, B. S. Caffo, and M. A. Lindquist. Improved estimation of subject-level functional connectivity using full and partial correlation with empirical bayes shrinkage. *NeuroImage*, 172:478–491, 2018.
- F. M. Miezin, L. Maccotta, J. Ollinger, S. Petersen, and R. Buckner. Characterizing the hemodynamic response: effects of presentation rate, sampling procedure, and the possibility of ordering brain activity based on relative timing. *Neuroimage*, 11(6):735–759, 2000.
- K. Müller, G. Lohmann, V. Bosch, and D. Y. Von Cramon. On multivariate spectral analysis of fmri time series. *NeuroImage*, 14(2):347–356, 2001.

- R. Nieuwenhuys, J. Hans, and C. Nicholson. *The central nervous system of vertebrates*. Springer, 2014.
- J. Rissman, A. Gazzaley, and M. D’Esposito. Measuring functional connectivity during distinct stages of a cognitive task. *Neuroimage*, 23(2):752–763, 2004.
- L. Tong, R.-W. Liu, V. C. Soon, and Y.-F. Huang. Indeterminacy and identifiability of blind identification. *IEEE Transactions on circuits and systems*, 38(5):499–509, 1991.
- N. Tzourio-Mazoyer, B. Landeau, D. Papathanassiou, F. Crivello, O. Etard, N. Delcroix, B. Mazoyer, and M. Joliot. Automated anatomical labeling of activations in spm using a macroscopic anatomical parcellation of the mni mri single-subject brain. *Neuroimage*, 15(1):273–289, 2002.
- R. Warnick, M. Guindani, E. Erhardt, E. Allen, V. Calhoun, and M. Vannucci. A bayesian approach for estimating dynamic functional network connectivity in fmri data. *Journal of the American Statistical Association*, 113(521):134–151, 2018.
- B. T. Yeo, F. M. Krienen, J. Sepulcre, M. R. Sabuncu, D. Lashkari, M. Hollinshead, J. L. Roffman, J. W. Smoller, L. Zöllei, J. R. Polimeni, et al. The organization of the human cerebral cortex estimated by intrinsic functional connectivity. *Journal of neurophysiology*, 2011.
- T. Zhang, F. Li, L. Beckes, and J. A. Coan. A semi-parametric model of the hemodynamic response for multi-subject fmri data. *NeuroImage*, 75:136–145, 2013.